ABSTRACT

Title of Document: Analysis of the Initial Spray from Canonical Fire Suppression Nozzles

Ning Ren, Master of Science, 2007

Directed By: Professor André Marshall, Department of Fire Protection Engineering

The performance of a fire suppression spray is governed by injector discharge characteristics. An atomization model based on the theoretical evolution of a radially expanding sheet generated by an impinging jet has been established in this study. The atomization model predicts characteristic initial drop location, size, and velocity based on injector operating conditions and geometry. These model predictions have been compared with measured discharge characteristics from three nozzle configurations of increasing geometrical complexity over a range of operating conditions. Differences between the predicted and measured initial spray are critically evaluated based on the experimentally observed atomization behavior.

Analysis of the Initial Spray from Canonical Fire Suppression Nozzles

By

Ning Ren

Thesis submitted to the Faculty of the Graduate School of the
University of Maryland, College Park, in partial fulfillment
of the requirements for the degree of
Master of Science
2007

Advisory Committee:
Professor André W. Marshall, Chair
Professor Arnaud Trouvé
Professor Peter B. Sunderland

Acknowledgements

Table of Contents

List of Figures

Nomenclature

A	Wave amplitude, m
A_0	Initial Wave amplitude, m
d	Drop diameter, μm
d^*	Dimensionless drop diameter
d_{lig}	Ligament diameter, μm
d_{v50}	Characteristic drop diameter, μm
D_{boss}	Boss diameter, mm
D_d	Deflector diameter, mm
D_{inlet}	Nozzle inlet diameter, mm
D_o	Orifice diameter, mm
f	Dimensionless wave amplitude
$f_{cirt,sh}$	Critical sheet break-up dimensionless wave amplitude
f_0	Critical sheet break-up dimensionless wave amplitude
g	Gravitational acceleration constant, m/s^2
h	Measurement elevation, m
K	K-factor of sprinkler, Lmin^{-1}bar$^{-1/2}$
l	Characteristic length, m
L_{inlet}	Length of nozzle inlet, mm
L_{jet}	Length of jet before deflector impact, mm
m_{lig}	Ligament mass, kg

n	Wave number
$n_{crit,sh}$	Sheet break-up critical wave number
$n_{crit,lig}$	Ligament break-up critical wave number
r	Radius, m
r_d	Deflector radius, m
r_d^*	Dimensionless deflector radius
$r_{bu,sh}$	Sheet break-up location, mm
$r^*_{bu,sh}$	Dimensionless sheet break-up location
S	Liquid gas friction term
T	Sheet thickness, m
T_d	Theoretical sheet thickness, m
T^*	Dimensionless sheet thickness
T_d^*	Dimensionless sheet thickness at the edge of deflector
$t_{bu,lig}$	Ligaments break-up time, s
U	Jet velocity, m/s
U_{sheet}	Sheet velocity
We	Weber number, $\rho_l U^2 D_o / \sigma$
We_{sheet}	Sheet Weber number, $\rho_l U_{sheet}^2 D_o / \sigma$
x	Coordinate
y	Coordinate
z	Coordinate

Greek letters

β	Thickening factor, T / T_0
σ	Surface tension, N/m
γ	Rosin-Rammler / log-normal correlation coefficient
λ	Wavelength
θ_{boss}	Angle of deflector boss, °
θ_{space}	Angle of deflector space, °
θ_{tine}	Angle of deflector tine, °
θ_{ini}	Initial sheet angle, °
ρ	Density, kg/m^3
μ	Dynamic viscosity, kg/ms
υ	Kinetic viscosity, m^2/s
ξ	Distance along the sheet, m
ω	Frequency, 1/s

Subcsripts

a	Air
i	Drop size bin
j	Measurement station
l	Liquid (water)

Chapter 1: Introduction

Fire safety is a world-wide issue that has challenged mankind for thousands of years. In ancient times, the only way to fight a fire was to use water. In modern times, with the help of technology, people have more choices. Carbon Dioxide and Halons have been introduced as an effective fire suppression alternative. However, recent environmental regulations have banned the use of Halon fire suppression agents because they destroy the ozone. Currently there is renewed interest in advancing water based fire suppression in the area of injector technology and modeling tools.

Sprinklers have been used for more than one hundred years. Compared to other fire suppression systems, sprinklers are cheap, reliable and easy to install, maintain and operate. Several studies have been conducted focusing on optimizing the drop size and mass flux distribution for optimal suppression performance. Other studies have focused on characterizing fire sprinklers by measuring these distributions. However, physical models for predicting the initial spray from sprinklers have yet to be developed. This chapter introduces the motivation for this project, reviews the previous work, and presents the objective for this study.

1.1 Motivation

The basic mechanisms for water-based fire suppression are clear, which can be summarized as cooling (fire gases and combustible material) and oxygen depletion. These suppression mechanisms are associated with the evaporation of the spray

introduced into the fire. The evaporation rate can be increased dramatically by atomizing the spray into small drops, increasing the surface area of the spray through atomizing water into fine drops. As more energy is absorbed by the spray, the temperature of the fire gases and combustible material will be decreased, effectively reducing the energy release rate. Alternatively, evaporation of water also displaces the oxygen available for burning, further reducing release rate.

Recognizing the importance of the spray characteristics in fire suppression performance, many spray focused experiments have been conducted. Unfortunately, these experiments are often limited to the measurement of global quantities evaluated in quiescent cool conditions. However, detailed spray characteristics are needed for use as CFD modeling input. Furthermore, the spray characteristics may change in actual operating conditions, which would include a hot turbulent environment and a range of injection pressures. A physics based model is needed to predict the details of the initial spray for injector performance analysis and integration with CFD tools.

1.2 Literature Review

Atomization is a complex flow problem, which has been extensively studied in a number of scientific and engineering disciplines, including propulsion, agricultural, chemical processing, and fire protection. Study of the atomization process has included analysis of internal flow interaction with the surrounding gas and stability analysis. Atomization configurations can be broadly categorized as sheet based or jet based. Due to the complexity of the atomization process, these configurations have

been studied both theoretically and experimentally. In the following section, previous research is reviewed from both theoretical and experimental perspectives.

1.2.1 Atomization Theory

When a liquid jet is injected into a gaseous fluid, it tends to break up into fragments due to surface tension and/or aerodynamic forces. Jet atomization was first studied by Rayleigh [1], who found that if the ambient gas and liquid viscosity were neglected, the jet is most susceptible to disturbances having wavelengths 143.7% of the jet circumference. A more sophisticated model was developed by Weber [2] in 1931, including the effect of liquid viscosity and density of the ambient gas. Weber's theory has been widely accepted; however, experiments conducted by Sterling and Sleicher [3] showed poor agreement with this theory. Furthermore, they pointed out that previous researchers had not fairly test Weber's theory, because their experiments used relatively long nozzles creating a velocity profile within the jet; an effect not included in the theory. However, they did not provide a method to predict the break-up of the jet considering the velocity profile effects.

On the other hand, atomization of liquid sheets was first studied by Savart in 1833 who observed break-up phenomena of radial expanding sheets produced by two co-axial colliding jets. It was demonstrated that when thin liquid sheets are generated in the atmosphere, unstable sinuous waves are formed. Squire [4] first solved the linearized equation for parallel liquid sheet instability. Hagerty and Shea [5] found that under normal operating conditions, the wavelength is relatively large compared

to the sheet thickness and their growth rates are consequently greater than those of the alternative dilatational forms typical of the jet atomization studied by Rayleigh.

Dombrowski [7-11] studied the effect of ambient density on drop formation in sheet based fan-spray nozzle experiments. He found that the drop size increases with ambient density. In his analysis, he assumed the relative velocity between sheet and ambient atmosphere is equal to the sheet velocity and that the flow in the sheet is irrotational. Thus, a velocity potential exists. By further assuming that the amplitude of the waves on the sheet is small compared to the sheet thickness and wavelength, a simplified linear ordinary differential wave growth equation was formulated. He defined dimensionless amplitude in the form of $f = \ln(A/A_0)$, and assumed the sheet would break up into ligaments every half wavelength at a critical dimensionless amplitude equal to 12. Further, he assumed the ligament would break up into droplet according to the simple Rayleigh instability mechanism. Dombrowski determined the fastest growing wave (most unstable) that caused the sheet to break up. For inviscid sheets, he determined $\lambda_{crit} = 4\pi\sigma/\rho_a U^2$, where σ is the surface tension of liquid and ρ_a is the density of ambient gas. He also suggested an approach for determining λ_{crit} for viscous sheets.

Li and Tankin [12-14] also studied the instability of two-dimensional viscous liquid sheets. They found that the surface tension always opposes the wave growth. In addition, they found that dilatational disturbances control the instability process for small Weber numbers, while sinusoidal disturbances dominate for large Weber numbers. However, they did not provide any data or criterion about sheet break-up.

4

Huang [15] studied the break-up of axisymmetric liquid sheets formed by the impingement of two co-axial jets. His results show the break-up distance of the sheet is a function of Weber number which is defined as $We = \rho U^2 d / \sigma$. He divided the break-up behavior into three regimes. The first regime occurs from $100 \leqslant We \leqslant 500$ characterized by a stable liquid sheet, in which the sheet break-up distance increases with We. The second regime occurs from $500 \leqslant We \leqslant 2,000$, which is called the transition regime. The third regime is defined from $2,000 \leqslant We \leqslant 30,000$, representing an unstable liquid sheet regime. In this regime, the break-up distance decreases following $We^{-1/3}$.

Clanet and Villermaux [16, 17] studied the break-up of liquid sheets generated by liquid jets impinging onto a small deflector. They studied the sheet break-up using water and ethanol and found result similar to Huang. In additional to liquid sheet break-up location, they found that the droplet mean arithmetic diameter follows the relationship of $d / D_0 = \rho^{*-2/3} We^{-1}$ for $1,000 \leqslant We \leqslant 2,000$ where $\rho^* = \rho_a / \rho_l$.

1.2.2 Spray Measurement

Droplet diameter, velocity and initial location are three essential quantities in the characterization fire suppression sprays. Theoretically, the mass flux distribution could be determined with the knowledge of the distributions of these three quantities. Early spray measurements were conducted using photographic techniques and laser shadowing method. Dundas [18] used these techniques to test six sprinklers with diameter ranging from 3.1 - 25.4 mm and with pressures ranging from 0.345 - 5.25

bar. The drop size was measured using a high-speed photographic technique. The photographs were analyzed both manually and using an electronic scanner. Dundas's results confirmed the correlation first proposed by Heskestad [19] that $d_{v50}/D_0 = CWe^{-1/3}$, where d_{v50} is the volumetric median diameter, D_0 is the orifice diameter, C is a constant depending on sprinkler geometry. Dundas summarized the C value from different researchers and showed $1.74 < C < 3.21$.

Yu [20] tested three upright sprinklers using a laser-based imaging technique for drop size measurement. He measured the drop size distribution at elevations of 3 m and 6 m below the sprinkler respectively. Measurements at these two elevations were almost the same, suggesting that these downstream measurements are useful for characterizing the initial spray in the absence of secondary atomization.

Detailed spray measurements have been conducted recently using advanced diagnostics such as Phase Doppler Interferometry (PDI) and Particle Image Velocimetry (PIV). The PDI method provides detailed local drop size and velocity information. Widmann [22] measured the drop size and velocity from actual sprinklers with K-factors from 43.5 L min^{-1} bar$^{-1/2}$ to 81.2 L min^{-1} bar$^{-1/2}$. He reported mean volume diameter, d_{30}, follows $We^{-1/3}$, except at low pressures (below 0.69 bar).

More recently, Sheppard [23] measured the drop velocities using the PIV technique. He presented his result in a spherical coordinate system with the sprinkler at the origin. He showed the variation of radial velocity with polar angle. He also provided a ball-park estimate of the radial velocity close to the sprinkler (~0.2m), which could be expressed as $U = 0.6(P/\rho_l)^{-1/2}$. Furthermore, Sheppard used the PDI technique to characteristic the drop size distribution. He measured the drop size at a

6

radial distance of 0.38 m at different azimuthal angle of 0º, 10º, 30º and 60º. However, due to the limitation of one point measurement, Sheppard did not provide an overall drop size distribution. Sheppard also studied the droplet trajectory; he calculated terminal velocities assuming spherical droplets, and found they agreed with his experiment.

The latest measurement was conducted by Blum [24], who measured the drop size distribution using a Spraytec Particle Analyzer developed by Malvern Instruments [47]. He measured the local drop size 1 m below the sprinkler at several radial locations. The overall drop size distributions were determined based on the mass flux and local drop size distribution measurements. Three sprinkler configurations were characterized in these experiments, which included a 'Basis' nozzle, a 'Tined' nozzle and a 'Standard' nozzle. The working pressure for these nozzles ranged from 0.69 bar to 2.76 bar. The results show that the drop size behavior is strongly related to the injector configuration, perhaps suggesting that different atomization modes may occur depending on the geometry.

1.2.3 Atomization Modeling

Atomization modeling is a task full of challenge because of the complexity of the atomization process, which is influenced by the nozzle geometry, working pressure, ambient air density, ambient temperature, as well as the internal injector flow structure.

Two methods are typically used to model the atomization process. The first approach is to use CFD with first-principle two-phase flow coupling. This approach requires simultaneous simulation of the liquid and gas phase flow with details. For simulating the two phases during atomization, Eulerian-Eulerian approach has been established [46]. The second lower fidelity approach uses surface stability analysis.

In the Eulerian-Eulerian approach, the different phases are treated mathematically as interpenetrating continua. Since the volume of a phase cannot be occupied by the other phase, the concept of phasic volume fraction is introduced. These volume fractions are assumed to be continuous functions of space and time and their sum is equal to one. Conservation equations for each phase are derived to obtain a set of equations, which have similar structure for all phases. These equations can be closed by providing constitutive relations that are obtained from empirical information.

Several models have been developed for multiphase flow problems. The VOF model is an Eulerian-Eulerian multiphase modeling approach that shows particular promise for free-surface flow. The VOF model uses a surface-tracking technique applied to a fixed Eulerian mesh. It is designed for two or more immiscible fluids where the position of the interface between the fluids is of interest. In the VOF model, a single set of momentum equations is shared by the fluids, and the volume fraction of each of the fluids in each computational cell is tracked through the domain. However, it should be noted that the sheet can be as thin as 100 microns just before break-up. In order to model the sheet break-up using the VOF method, the grid size must be much smaller than the sheet thickness, which increases the computation time

greatly. This resolution requirement prohibits the VOF technique for use as a practical tool for predicting atomization in fire suppression sprays.

Although detailed information could be obtained from numerical simulation using multi-dimensional multi-phase flow models, this method is not a practical solution for predicting the initial spray (atomization) for engineering applications, especially if there are numerous sprinklers/nozzles. An alternative method for CFD applications is to use surface stability theory describing wave dispersion on the liquid sheet. Starting with a force balance on the liquid sheet and assuming a wavy liquid-gas interface, the wave dispersion equations can be determined in terms of a dimensionless wave growth rate or dimensionless wave amplitude. Several research studies have developed wave dispersion equations for various geometries using similar assumptions. These equations are used to characterize the wave growth rate or amplitude predicting break-up or atomization at some critical conditions. The break-up criterion is established experimentally and may change with nozzle configurations.

1.3 Research Objectives

The current study builds on fire suppression spray modeling ideas established by Di [26, 45]. A series of modeling modifications have been introduced in the current research to improve the fidelity of the model. Simplified scaling laws have also been developed from the modeling theory to facilitate analysis. Discharge characteristics from 'canonical' fire suppression nozzles were also obtained during this study with Blum [24]. These full scale tests provide a detailed description of the

initial spray in well characterized geometries. Comparisons are made between the detailed initial spray data and the refined model predictions to evaluate the model and identify focus areas for improvements.

Chapter 2: Approach

In CFD applications, a variety of models are needed to simulate the physical process associated with fire suppression. In practical analysis, fire suppression is initiated with a nozzle activation model which controls the start of the spray based on a prescribed activation condition. After activation, a spray atomization model can be used to define the characteristics of the initial spray. These characteristics include the droplet diameter, initial droplet location, and droplet velocity. The initial spray data will be used as input to a spray dispersion model which predicts the trajectory of droplets including the thermal, mass, and momentum interaction of the dispersed phase (liquid) with the continuous phase (gas). An extinction model is also necessary to simulate the effects of oxygen depletion on combustion and thermal effects. Although proper specification of the initial spray is essential for CFD analysis of fire suppression, atomization models have received limited attention for this application. In CFD software such as FDS, correlations are used instead of atomization models [48]. These correlations are obtained from limited full spray test conducted almost ten years ago. The initial spray characteristics are strongly dependent on the sprinkler configuration and the result of limited tests cannot be faithfully applied to all sprinklers. Current correlations are limited for a variety of reasons. For instance, the initial drop diameter, location and velocity correlate strongly; however, current correlations do not capture this coupling. The correlations are also based on cool ambient experiments and do not include the effect of the ambient density reduction occurring in fires which will likely influence the atomization process and the resulting

drop size. Based on essential atomization physics, a model is under development to predict the characteristics of the initial spray. This chapter will discuss the general physics of the atomization process in detail based on previous work and atomization measurements performed by Blum [24] and Ren. A new scaling law developed in this study is also explored.

2.1 Atomization Physics

The atomization process can be divided into four distinct stages as shown in Figure 1. They are the sheet formation, sheet trajectory, sheet break-up and ligament break-up stages.

The modeling of atomization is actually a problem of multiphase flow, which can be solved with multiphase models. Two distinct of multiphase flow problems
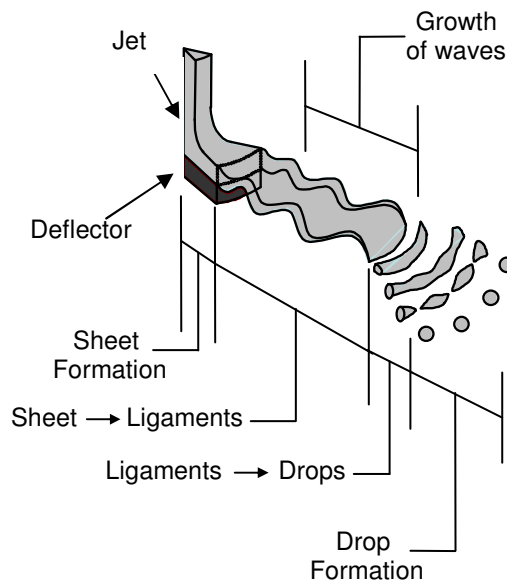

Figure 1. Description of atomization process [26]

arise in fire suppression applications. In the first stage, an immiscible liquid sheet is formed; the interaction of the liquid sheet and ambient air is a problem of free surface flow. After the continuous liquid sheet breaks up into ligaments and droplets, the problem becomes one of a discrete fluid phase in a continuous gas. Although first principle multiphase flow models have been established, they are not suitable for engineering level study (see §1.2.3). The approach used in this chapter is based on stability theory.

2.1.1 Sheet Formation

Generally, the liquid sheet is formed by impinging a liquid jet onto a deflector. Difference sprinkler configurations are mainly treated by changes in the deflector geometry. Those differences could change the thickness and velocity of the liquid sheet which will change initial spray characteristics.

Three types of sprinklers are analyzed in this chapter. The thickness and velocity are determined from Watson's theory [28] based on free-surface similarity boundary-layer concept. Figure 2 shows the formation of liquid sheet, which is characterized by four stages.

Region I: Impinging region ($r < D_0 / 2$). The direction of water jet is changed in this region from vertically to radially. A radial expanding sheet is formed. There is a stagnation point in the center of the impinging region. In this region, a growing boundary layer has not been formed; the sheet velocity can be approximated as the free jet velocity, U_{jet}.
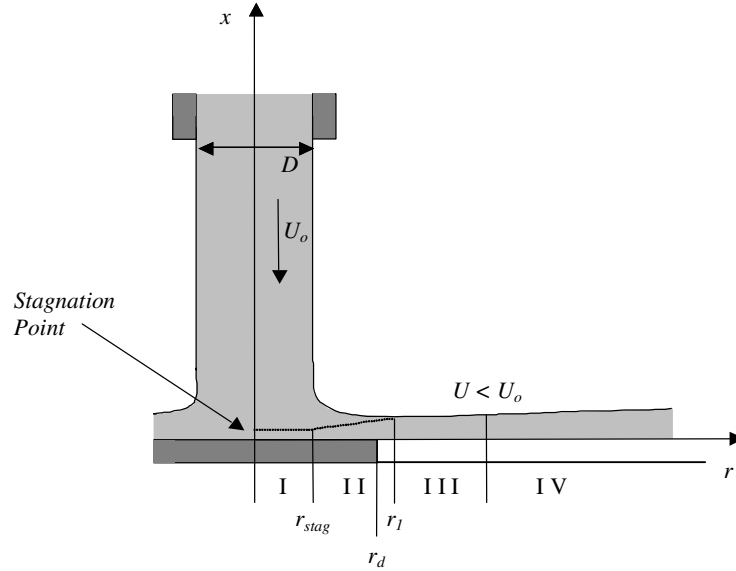
Figure 2. Sheet formation from impinging jet [26]

Region II: Boundary-layer developing region ($D_0/2 < r < r_l$). In this region the boundary-layer keeps growing with a Blasius velocity profile. In this region, the boundary-layer thickness is less than the sheet thickness until at the end of this region, where the boundary-layer reaches the free surface ($r = r_s$).

Region III: In this region ($r > r_s$), the free surface velocity is slightly smaller than U_0, but nearly constant and the velocity profile is predicted by a Blasius.

Region IV: Quickly decreasing free surface velocity and the boundary-layer affects the whole sheet. The velocity decreases greatly and the velocity profile is given by a non-Blasius similarity solution.

In order to show the effect of viscous interaction with the deflector, a non-dimensional sheet thickness is defined as the actual thickness compared to an inviscid sheet thickness solution, which is given by

$$\beta = \frac{T}{T_0}, \tag{2-1}$$

where $T_0 = D_0^2/8r$. Typically, the working pressure of a nozzle is above 0.345 bar, and the jet velocity $U_0 > 5$ m/s. The internal diameter of the nozzle D_0 is larger than 8 mm. The Reynolds number of the jet is on the order of 10^4, indicating the flow is in the turbulent regime. Following Watson, in Region II where $r < r_l$, the sheet thickness is given by

$$T(r)|_{\text{Region I}} = \frac{D_0^2}{8r} + 0.0245 D_0^{1/5} r^{4/5}/\text{Re}^{1/5} , \tag{2-2}$$

where Re is Reynolds number. The boundary-layer thickness, δ, is

$$\delta = 0.303 D_0^{1/5} r^{4/5}/\text{Re}^{1/5}. \tag{2-3}$$

The boundary of Region II is

$$r_l = 0.183 D_0 \text{Re}^{1/3}. \tag{2-4}$$

In Region III where $r > r_l$, the sheet thickness is

$$T(r)|_{\text{Region II}} = 1.022 \frac{D_0^2}{8r} + 0.0224 \frac{r^{5/4}}{(D_0 \text{Re})^{1/4}}, \tag{2-5}$$

where Q is the flow rate, l is an arbitrary constant length

$$l^{9/4} = 5.71 \text{Re}^{1/4} D_0^{9/4}. \tag{2-6}$$

The non-dimensional form of boundary-layer thickness and sheet thickness is

$$\beta = \begin{cases} 1 + 0.196 \text{Re}^{-1/5}\left(\dfrac{r}{D_0}\right)^{9/5} & r < r_l \\[4mm] 1.022 + 0.179 \text{Re}^{-1/4}\left(\dfrac{r}{D_0}\right)^{9/4} & r > r_l \end{cases}. \tag{2-7}$$

From conservation of mass, the average velocity of sheet at the edge of deflector is determined by

$$U = \frac{D^2}{8r_d h_d} U_0 = \frac{Q}{2\pi r_d h_d} = \frac{Kp^{1/2}}{2\pi r_d h_d}, \qquad (2\text{-}8)$$

where K is the K-factor of the sprinkler in unit of $Lmin^{-1}bar^{-1/2}$.

The most important parameter in sheet formation is the sheet thickening factor β and average sheet velocity U. The sheet velocity governs the wave growth rate and the sheet thickness determines the diameter of the droplet. It is also worth noting that the velocity profile of the sheet will have some influence on the sheet break-up. To simplify the problem, in the following analysis, the average sheet velocity is used instead of using velocity profile [3].

2.1.2 Sheet Trajectory

After leaving the deflector, the external forces acting on the liquid sheet are only the friction force and gravity force. Distinct from a discrete object (i.e. droplet), the liquid sheet is a continuous expanding stream, which has a more complex trajectory. Furthermore, the thickness of the sheet changes as the sheet expands radially outwards. Internal forces also affect the trajectory of the sheet especially when the liquid sheet is very thin and the curvature of the trajectory is large. To determine the trajectory of the sheet, a group of differential equations are provided by Ibrahim [25] with consideration of all possible parameters.

The model is based on curvilinear body-fitted coordinates as shows in Figure 3 where r and z are the radial and vertical coordinate of the cylindrical coordinate system. The variable ξ is the position in curvilinear body-fitted coordinate, η is the
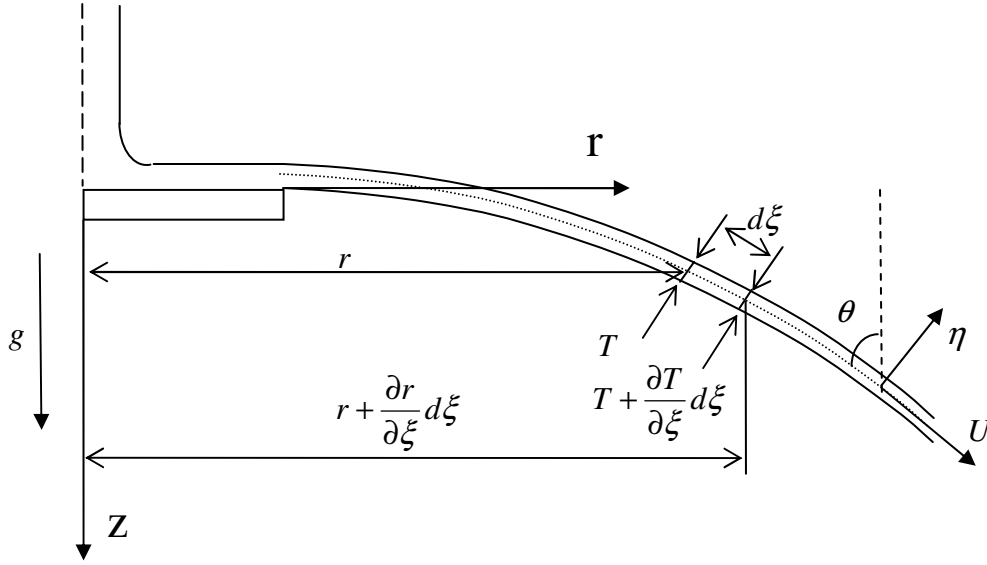
Figure 3. Description of sheet trajectory

coordinates normal to the sheet, T is the local sheet thickness, U is the local sheet velocity, θ is the angle between the median streamline and axial direction z, and g is the gravitational acceleration constant. The problem simplified by using the curvilinear body-fitted coordinates. For the radial expanding sheet, the continuity and momentum equations could be simplified as

Continuity:

$$\frac{\partial}{\partial \xi}\left(\rho_l UrT\right) = 0 \tag{2-9}$$

Momentum in stream-wise direction:

$$\rho_l U \frac{\partial U}{\partial \xi} = S + \rho_l g \cos\theta \tag{2-10}$$

Momentum in direction vertical to the sheet:

$$\rho_l U^2 \frac{\partial \theta}{\partial \xi} = -\frac{\partial P_l}{\partial \eta} - \rho_l g \sin\theta, \tag{2-11}$$

where P_l is the pressure difference between the two sides of the sheet, S is the liquid gas interaction friction term given by

$$S = -\frac{\rho_a}{2T}[0.79(1+150T/r)\,\mathrm{Re}^{-1/4}](U_a - U)^2, \qquad (2\text{-}12)$$

where ρ_a is the gas density, U_a is the gas velocity, Re is the Reynolds number defined as $Re = 2\rho_a r_d \,|U_a - U|/\mu_a$. The induced gas velocity should be coupled with the velocity of the sheet, which introduces extra equations for gas. Actually, the gas induced velocity is much smaller than the moving sheet. Assuming zero gas velocity is a reasonable simplification.

The term P_l is the pressure difference across the sheet given by

$$\frac{\partial P_l}{\partial \eta} \approx \frac{\Delta P_l}{T} = \frac{\Delta P_g}{T} + \frac{2\sigma}{T}\left(\frac{\cos\theta}{r} - \frac{\partial\theta}{\partial\xi}\right), \qquad (2\text{-}13)$$

where ΔP_g is the gas pressure difference between the sheet. In this case, ΔP_g is zero; the extra pressure is introduced only by surface tension forces.

To close the system, two more equations are needed which are provided by the coordinate transformation from cylindrical to body-fitted coordinates. In the r direction, it is

$$\frac{dr}{d\xi} = \sin\theta, \qquad (2\text{-}14)$$

and in the z direction, it is

$$\frac{dz}{d\xi} = \cos\theta. \qquad (2\text{-}15)$$

Now we have five variables, which are U, T, θ, r, z and five differential equations which are summarized below

$$\begin{cases} rT\dfrac{dU}{d\xi}+UT\dfrac{dr}{d\xi}+Ur\dfrac{dT}{d\xi}=0 \\[2ex] \rho_l U\dfrac{dU}{d\xi}=-\dfrac{\rho_a U^2}{2T}[0.79(1+150T/r)\operatorname{Re}^{-1/4}]+\rho_l g\cos\theta \\[2ex] \rho_l U^2\dfrac{d\theta}{d\xi}=-\dfrac{2\sigma}{T}\left(\dfrac{\cos\theta}{r}-\dfrac{d\theta}{d\xi}\right)-\rho_l g\sin\theta \\[2ex] \dfrac{dr}{d\xi}=\sin\theta \\[2ex] \dfrac{dz}{d\xi}=\cos\theta \end{cases} \qquad (2\text{-}16)$$

We also need five boundary conditions to solve the equation. They are given when ξ is zero,

$$\begin{cases} U\mid_{\xi=0}=U_{sheet} \\ T\mid_{\xi=0}=T_d \\ \theta\mid_{\xi=0}=\theta_{ini} \\ r\mid_{\xi=0}=r_0 \\ z\mid_{\xi=0}=0 \end{cases} \qquad (2\text{-}17)$$

The boundary conditions of sheet velocity and thickness are provided by the jet model. Because there are no good models to predict the initial angle, the initial angle is currently determined experimentally. It is not possible to solve the non-linearly equations analytically, a fourth order Runge-Kutta method is used to find the solution of U, T, θ, r, z. The purpose of the trajectory model is to predict the local sheet thickness and sheet velocity. In previous atomization studies, the sheet velocity was regarded as a constant by all researchers and the sheet thickness was also treated as a simple function of radius. The trajectory model provides those values in a more accurate way which will be used in the sheet break-up model.

2.1.3 Sheet Break-up

The radial expanding liquid sheet is inherently unstable and the sheet behavior is typically attributed to a Kelvin-Helmholtz type of instability producing a flapping sheet. An analysis of the mathematical description of the flapping sheet provides some insight into the nature of the flag-like instability.

First, the wave form on the growing sheet is explored. This exercise will be followed by a stability analysis to determine the critical condition for sheet break-up. The form of the initial disturbance is

$$y = y_0 \exp(i(nx - \omega t)), \qquad (2\text{-}18)$$

where $n = n_r + in_i$ and $\omega = \omega_r + i\omega_i$ are wave number and frequency respectively. If the solution of n is a complex number, the wave is spatially unstable where n_i is the spatial growth rate, which corresponds to a convective instability. If the solution of ω is a complex number, the wave is temporally unstable where ω_i is the temporal growth rate, which corresponds to an absolute instability. Sheet break-up experiments show that the wave amplitude changes with location and not with time, indicating a spatial instability. The wave equation simplifies to

$$y = y_0 \exp(n_i x)\sin(n_r x - \omega_r t), \qquad (2\text{-}19)$$

Figure 4 shows the waves and ligaments formed form the sheet at different times.

Four forces are essential for the development of the flapping sheet instability; they are the pressure force, friction force, surface tension force and viscous force. Subject to these forces, waves will grow on the smooth liquid sheet like a flapping flag. Sinuous waves and dilatational waves are possible. When the amplitude of the waves is large enough, the continuous sheet may break up into a ring like ligament.
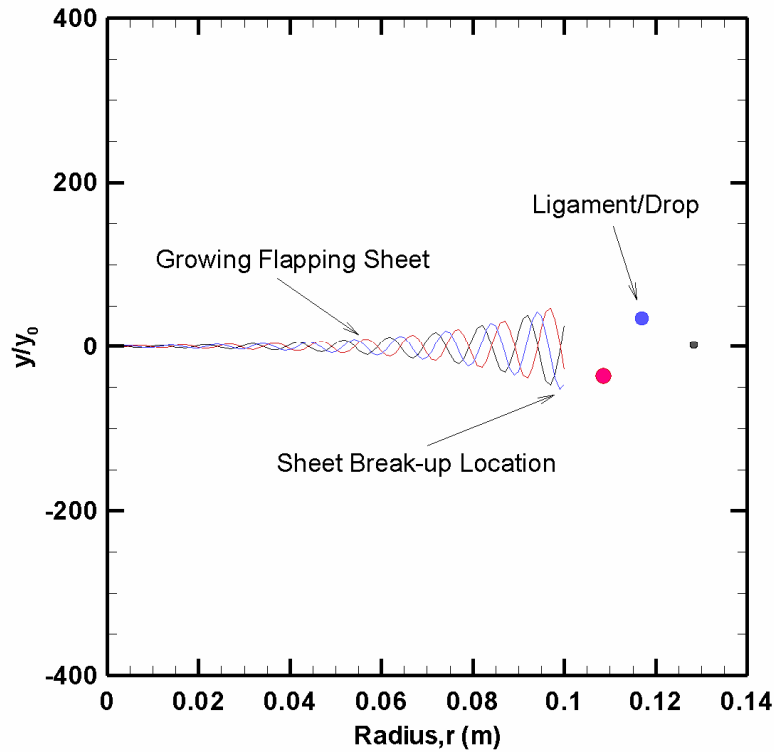
Figure 4. Growing wave on the sheet; ——*t1;* ——*t2;* ——*t3*

The wavelength at break-up governs the ligament diameter. A theory based on linear stability has been developed by Dombrowski [8] to predict the wave instability for two dimensional waves in an inviscid gas. In his model, he assumes the flow is irrotational. A velocity potential is used to describe the flow motion. By further assuming the wave amplitude is small compared to the wavelength, the free boundary condition can be simplified. In the viscous force term, there are contributions from normal shear force and sheet thinning. However, Dombrowski estimated that the thinning term is small compared to other forces, and if the wave number is sufficiently large, this term can be neglected. This simplification results in a

straightforward model to predict the break-up of the radial expanding sheet. The simplified equation to describe the wave growth on the sheet is given by

$$\left(\frac{\partial f}{\partial t}\right)^2 + \frac{\mu_l}{\rho_l} n^2 \left(\frac{\partial f}{\partial t}\right) - \frac{2(\rho_a n U^2 - \sigma n^2)}{\rho_l T} = 0, \qquad (2\text{-}20)$$

where t is time, f is a dimensionless wave growth defined by $f = \ln(A / A_0)$, A is the wave amplitude and A_0 is initial wave amplitude, μ_l is the liquid viscosity, T is sheet thickness, n is wave number defined by $n = 2\pi / \lambda$, and λ is wavelength.

The sheet velocity, U, and sheet thickness, T, is given by the trajectory model. Actually, the trajectory and sheet break-up analysis are only weakly coupled. According to the linear wave dispersion theory, the wave amplitude is small compared to the wavelength. The effect of waves on the sheet trajectory can be neglected. However, the sheet thickness and velocity significantly affect the wave growth rate.

Form the wave dispersion equation, we can see that the viscous force and surface tension force is always playing an opposite role on the wave growth. The pressure force accelerates the wave growth. As the density ratio, $\rho^* = \rho_a / \rho_l$ increases, the wave growth rate increases. In real fire scenarios, the gas temperature increases and the density decreases. As a result, the wave growth rate will decrease.

Although the wave number, n, can be any real number, there is only one wave number that makes the wave grow the fastest. This wave number is called the critical wave number, n_{cirt}, which is considered to be the most unstable wave that will first lead to break-up. The sheet won't break-up until f reaches to critical dimensionless wave amplitude $f_{crit,sh}$. In Dombrowski's theory, $f_{crit,sh}$ is a constant with a value of

22

12 regardless of working condition. Other researchers also found that $f_{crit,sh}$ is a constant which is close to 12. It should be noted that in our experiment, $f_{crit,sh}$ was assumed to be a function of nozzle configuration and could be determined by experiment. However, it should be noticed that for viscous thinning sheet, it is not available to get the critical wave number analytically, which must be determined form iterating integral of f. The break-up time is recorded when f reaches $f_{crit,sh}$. And from the trajectory model, the corresponding sheet velocity, sheet thickness, and the break-up location $r_{crit,sh}$ are found according to the break-up time.

The thin flapping sheet is assumed to break up into ring-like fragments having a radial extent of half wavelength. From conservation of mass, the fragment of ligament mass is determined by

$$m_{lig} = \pi \rho_l T_{bu,sh} [(r_{bu,sh} + \pi / n_{crit,sh})2 - r^2{}_{bu,sh}] . \qquad (2\text{-}21)$$

Assuming the cross-section of the ligament is circular, the equivalent diameter can be determined from the Eq. (2-22)

$$m_{lig} = \pi^2 \rho_l \frac{d^2{}_{lig}}{2} \left(r_{bu,sh} + \frac{d_{lig}}{2} \right) . \qquad (2\text{-}22)$$

The ligament diameter is not only related to the ligament mass, but also related to the sheet break-up location. The sheet break-up analysis reveals that the critical wave number and sheet break-up location are important quantities governing atomization behavior. In this study, the sheet break-up location is carefully measured for evaluation of the atomization model.

2.1.4 Ligament Break-up

The ligaments produced by the sheet are also unstable. Different from the sheet break-up model, the surface tension force plays a positive role for the wave growth. Weber gave the analysis of ligament break-up, similar to the sheet break-up; there is also a critical wave number which is given by

$$n_{cirt,lig} d_{lig} = \left[\frac{1}{2} + \frac{3\mu_l}{2(\rho_l d_{lig}\sigma)^{1/2}} \right]^{1/2}.$$

(2-23)

Usually, the diameters of the ligaments are on the order of 10^{-4} to 10^{-3} m. For water, the second term in the brackets is about 0.006 to 0.002, which is negligible compared to 0.5. The unstable waves on the ligament are dilational waves, which will lead to break-up every one wavelength. From conservation of mass, the droplet diameter can be expressed as

$$d = d_{lig}^{2/3} \left(\frac{3\pi}{n_{crit,lig}} \right)^{1/3}.$$

(2-24)

Combining Eq. (2-22) and Eq. (2-24), the final expression for droplet can be simplified as

$$d = 1.88 d_{lig}.$$

(2-25)

The time needed for ligaments to break-up into droplets is given by

$$t_{bu,lig} = 24 \left(\frac{2\rho_l}{\sigma} \right)^{1/2} \left(\frac{d_{lig}}{2} \right)^{3/2}.$$

(2-26)

With the knowledge of the sheet break-up location, initial velocity of the ligament, and break-up time of the ligament, the initial droplet location is easily found. For example, the initial radial drop location is given by

24

$$r_{drop} = r_{bu,sh} + U_{lig} t_{bu,lig}$$ (2-27)

Here, the velocity of ligament is considered as a constant provided by the sheet velocity at break-up. Also any changes to the trajectory of the ligament are neglected.

2.2 Numerical Model

In §2.1, the important physics and associated governing equations for atomization in the impinging jet configuration were prescribed. The equations describing the break-up process are too complex to solve analytically. However, a numerical model consisting of four sub-models corresponding to the four important physical processes described in §2.1 has been developed in this study. A diagram describing the model is included in Figure 5 and a detailed summary of equations and modeling parameters are include in Appendix A. This numerical model provides deterministic or stochastic formulations for predicting the initial spray.
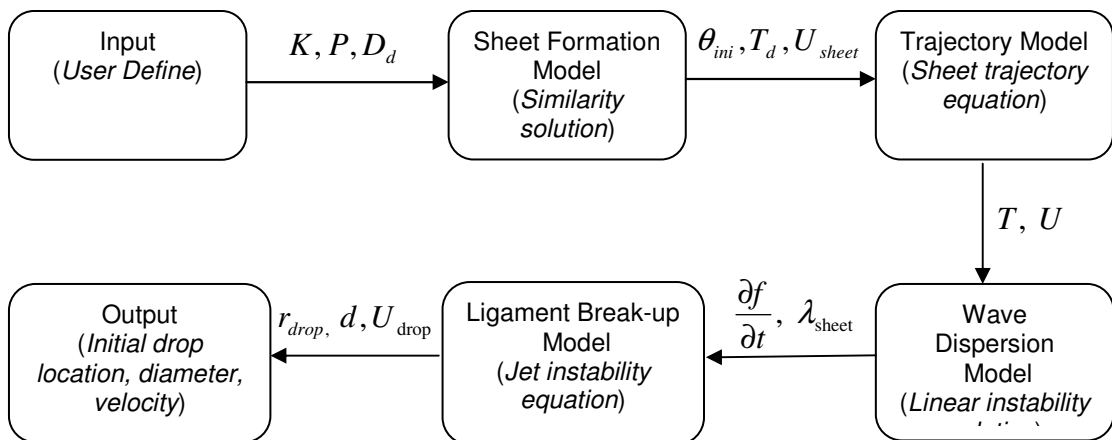

Figure 5. Deterministic description of atomization model

The Deterministic model only provides characteristic initial spray quantities. However, fire suppression sprays show strong stochastic behavior. For example, the sheet does not always break-up at the same distance and the droplets do not have only one diameter. In order to model these stochastic behaviors, probability distributions are introduced into the model to treat the various stages of the break-up process. The sheet critical break-up amplitude, the sheet break-up wavelength, and the ligament break-up wavelength are all treated stochastically. This physics-based technique provides an alternative to specifying a standard distribution about a calculated characteristic drop size. The stochastic model ultimately provides distributions for initial drop size and location. A detailed discussion on the stochastic model is provided by Di [26, 45] and repeated in Appendix B.

2.3 Scaling Law

The scaling laws for sheet break-up and droplet diameter are based on the equations in § 2.1 and Appendix B. The scaling laws for sheet break-up use the inviscid assumption which greatly simplifies the scaling expressions. This assumption is a reasonable approximation for a low viscosity fluid like water ($\mu = 0.0011 \text{N/m}^2\text{s}$). A group of dimensionless parameters are used to express the scaling laws. These parameters include

$\rho^* = \rho_a / \rho_l$ Dimensionless Density

$We = \rho_l U_{jet}^2 D_0 / \sigma$ Jet Weber Number

$$r_d^* = r_d / D_0 \qquad\qquad \text{Dimensionless Deflector Radius}$$

$$r_{bu,sh}^* = r_{bu,sh} / D_0 \qquad\qquad \text{Dimensionless Sheet Break-Up Distance}$$

$$T_d^* = T_d / D_0 \qquad\qquad \text{Dimensionless Sheet Thickness at Deflector Edge}$$

$$d^* = d / D_0 \qquad\qquad \text{Dimensionless Droplet Diameter}$$

$$\beta = T / T_0 \qquad\qquad \text{Thickening Factor}$$

The Weber number based on the sheet velocity is smaller than the jet Weber number, We, due to viscous deceleration along the deflector and drag forces from the surrounding air, which is

$$We_{U_{sh}} = \frac{We}{\beta^2} . \qquad\qquad (2\text{-}28)$$

The expression for wave number from the viscous dispersion equation is too complex for scale analysis. To simplify the analysis, an inviscid model is used assuming the viscosity of liquid is zero. The wave dispersion Eq. (2-20) simplifies to

$$\left(\frac{\partial f}{\partial t}\right)^2 - \frac{2(\rho_a n U_{sheet}^2 - \sigma n^2)}{\rho_l T} = 0 . \qquad\qquad (2\text{-}29)$$

Since the wave is growing all the time until break-up, $\partial f / \partial t$ will always be a positive number and can be expressed as

$$\frac{\partial f}{\partial t} = \left(\frac{2(\rho_a n U_{sheet}^2 - \sigma n^2)}{\rho_l T}\right)^{\frac{1}{2}} . \qquad\qquad (2\text{-}30)$$

By taking the derivative of Eq. (2-30) with respect to n, the critical wave number can be found when $\partial(\partial f / \partial t)/\partial n \,|_{n_{crit,sh}} = 0$, which yields the maximum growth rate

$$n_{crit,sh} = \frac{\rho_a U_{sheet}^2}{2\sigma} . \qquad\qquad (2\text{-}31)$$

The sheet critical wave number can also be expressed as

$$n_{crit} = \frac{\rho_a U_{sheet}^2}{2\sigma} = \frac{\rho_a We}{2\rho_l D_0 \beta^2} = \frac{\rho^* We}{2D_0 \beta^2}.$$ (2-32)

The dimensionless wave growth rate will be

$$\frac{\partial f}{\partial t} = \rho^* U_{sheet} \left(\frac{We}{2D_0 T \beta^2} \right)^{\frac{1}{2}}$$

$$= \rho^* U_{sheet} \left(\frac{rWe}{2D_0 r_d T_d \beta^2} \right)^{\frac{1}{2}},$$ (2-33)

From the expression of $r = r_d + U_{sheet} \cos\theta_{ini} t$, where θ_{ini} is the sheet initial angle, which is a function of sprinkler configuration. We can find that $dr = U_{sheet} \cos\theta_{ini} dt$. And the wave growth equation can be expressed in terms of radius as

$$\frac{\partial f}{\partial t} = \frac{\partial f}{\partial r} U_{sheet} \cos\theta_{ini} = \rho^* U_{sheet} \left(\frac{rWe}{2D_0 r_d T_d \beta^2} \right)^{\frac{1}{2}},$$ (2-34)

$$\frac{\partial f}{\partial r} = \frac{\rho^*}{\cos\theta_{ini}} \left(\frac{rWe}{2D_0 r_d T_d \beta^2} \right)^{\frac{1}{2}}.$$ (2-35)

At the end of integral, the dimensionless amplitude reaches the critical value. In this study, the critical amplitude is a function of nozzle configuration, and in the following analysis, f_0 is used instead of f_{crit}, where

$$f_0 = \frac{2}{3} \frac{\rho^*}{\cos\theta_{ini}} \left(\frac{We}{2D_0 r_d T_d \beta^2} \right)^{\frac{1}{2}} \left(r_{bu,sh}^{3/2} - r_d^{3/2} \right).$$ (2-36)

Finally, the dimensionless sheet break-up distance can be expressed as

$$\frac{r^*_{bu,sh}}{r^*_d} = \left(1 + \frac{3f_0 \cos\theta_{ini}}{2\rho^* r^*_d}\left(\frac{2T^*_d \beta^2}{We}\right)^{\frac{1}{2}}\right)^{\frac{2}{3}}. \tag{2-37}$$

Eq. (2-37) shows the break-up distance is a complex function of Weber number.

However, the equation can be simplified if $\frac{3f_0 \cos\theta_{ini}}{2\rho^* r^*_d}\left(\frac{2T^*_d \beta^2}{We}\right)^{\frac{1}{2}} \gg 1$, which means

the sheet break-up distance is much larger than the radius of the deflector. Under this

condition, the dimensionless sheet break-up distance is given by

$$\frac{r^*_{bu,sh}}{r^*_d} = \left(\frac{3f_0 \cos\theta_{ini}}{2\rho^* r^*_d}\right)^{2/3} \left(2T^*_d \beta^2\right)^{1/3} \left(We\right)^{-1/3}. \tag{2-38}$$

For the same nozzle, the sheet break-up distance would follow $We^{-1/3}$.

Since we already have the wave number and sheet break-up distance, the

diameter of the ligament can be found. Because the sheet break-up distance is much

larger than the sheet wavelength, the ligament mass can be simplified as

$$\begin{aligned} m_{lig} &= \pi\rho_l T_{bu,sh}[(r_{bu,sh} + \pi/n_{crit,sh})^2 - r^2_{bu,sh}] \\ &\approx 2\pi^2 \rho_l T_{bu,sh} r_{bu,sh}/n_{crit,sh} \end{aligned}. \tag{2-39}$$

The ligament mass is a function of ligament diameter, which is also much smaller

than the sheet break-up distance. Thus, the Eq. (2-22) will be simplified as

$$m_{lig} \approx \pi^2 \rho_l \frac{d^2_{lig}}{2} r_{bu,sh}, \tag{2-40}$$

Combining Eq. (2-39) and Eq. (2-40), the ligament diameter will be

$$d_{lig} \approx 2\left(\frac{T_{bu,sh}}{n_{crit,sh}}\right)^{\frac{1}{2}} = 2\left(\frac{D_0 r_d T_d \beta^2 \cos\theta_{ini}}{r_{bu,sh}\rho^* W_e}\right)^{\frac{1}{2}}, \tag{2-41}$$

From Eq. (2-25), the final expression for droplet diameter is given by

$$d = 1.88 d_{lig} = 3.76 \left(\frac{D_0 r_d T_d \cos \theta_{ini}}{r_{bu,sh} \rho^* We} \right)^{\frac{1}{2}}$$

$$= 3.76 \frac{\left(D_0 r_d T_d \beta^2 \cos \theta_{ini} \right)^{\frac{1}{2}}}{\left(r_d^{3/2} + \frac{3 f_0 \cos \theta_{ini}}{2 \rho^*} \left(\frac{2 D_0 r_d T_d \beta^2}{We} \right)^{\frac{1}{2}} \right)^{\frac{1}{3}} \left(\rho^* We \right)^{\frac{1}{2}}} . \qquad (2\text{-}42)$$

The dimensionless form of droplet diameter is

$$d^* = \frac{d}{D_0} = 3.76 \frac{\left(T_d^* \beta^2 \cos \theta_{ini} \right)^{\frac{1}{2}}}{\left(1 + \frac{3 f_0 \cos \theta_{ini}}{2 \rho^* r_d^*} \left(\frac{2 T_d^* \beta^2}{We} \right)^{\frac{1}{2}} \right)^{\frac{1}{3}} \left(\rho^* We \right)^{\frac{1}{2}}} . \qquad (2\text{-}43)$$

If the break-up distance is much larger than the radius of deflector, that

is $\frac{3 f_0 \cos \theta_{ini}}{2 \rho^* r_d^*} \left(\frac{2 T_d^* \beta^2}{We} \right)^{\frac{1}{2}} \gg 1$, the dimensionless droplet diameter is simplified to

$$d^* = 3.5 \left(\rho^* \right)^{-1/6} \left(\cos^{1/2} \theta_{ini} \frac{r_d^* T_d^* \beta^2}{f_0} \right)^{1/3} \left(We \right)^{-1/3} . \qquad (2\text{-}44)$$

All the possible factors which affect the droplet diameter are included in Eq. (2-44). There are two coefficients for the Weber power law provided in Eq. (2-44); the first one is the dimensionless density. Increasing the air density will decrease the droplet diameter. In a real fire, the air density is reduced; we can conclude that the droplet diameter will increase. The second coefficient is the sprinkler configuration. For the same sprinkler, this term is almost a constant. The *We* is determined by the jet diameter and working pressure. Increasing the working pressure will decrease the drop diameter following *We$^{-1/3}$*.

Chapter 3: Results and Analyses

3.1 Experiment Description

Experiments including sheet trajectory, sheet break-up and drop size measurements were performed to characterize the initial spray for evaluation of the atomization model and related scaling laws. A detailed discussion of the experimental techniques used for these experiments can be found in Blum [24]. These experiments were systematically conducted in nozzles of increasing complexity to gain insight into the effect of nozzle geometry on the atomization process. Three nozzle configurations were investigated in this study identified as the basis, tined, and standard nozzles. The basis nozzles consisted of a separate injector and deflector disk (three different injectors sizes were used in this study). The tined nozzle is used to isolate the effect of the tines and spaces on the deflector. The nozzle was fabricated by removing the boss from a standard Tyco D3 nozzle creating a flat notched
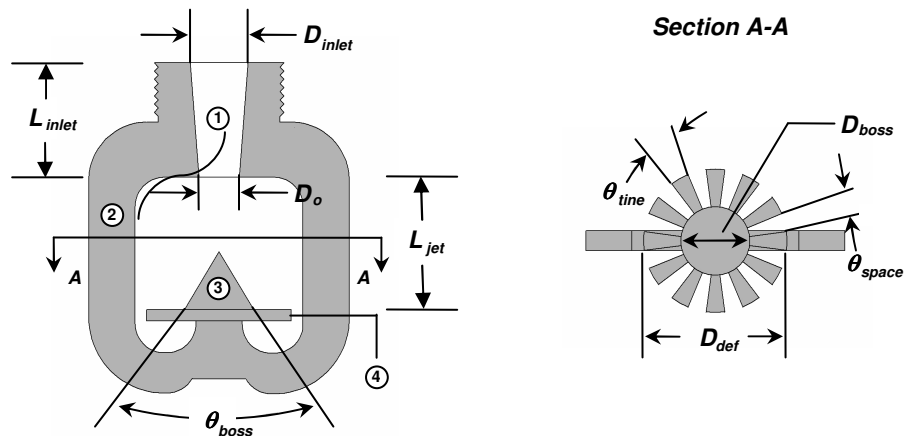

Figure 6. Standard nozzle configuration (Tyco D3 fire suppression nozzle); (1) Inlet (2) Frame Arms (3) Boss (4) Deflector [24]

deflector. A conventional Tyco D3 nozzle shown in Figure 6 was used for the standard nozzle adding boss effects and representing a practical configuration. Table 1 summarizes the important geometries and flow characteristics for the three nozzles used in this study.

3.2 Model Evaluation

In this section, the preliminary results of atomization modeling will be discussed. The atomization model is divided into several sub-models, each of which corresponds to a physical stage of the atomization process. Each of the sub-models will be evaluated with comparison to available experimental data.

Table 1. Sprinkler Configuration [24]

	ΔP (bar)	U_{jet} (m/s)	Basis Nozzle			Tined Nozzle		Standard Nozzle	
			$D_o = 3.5$	$D_o = 6.7$	$D_o = 9.7$	Tine (0°)	Space (15°)	Tine (0°)	Space (15°)
Initial Angle, θ (°)	0.69	11.8	9.47	4.00	3.99	4.56	N/A	2.67	N/A
	1.38	16.6	7.87	4.19	3.50	4.03	N/A	4.05	N/A
	2.07	20.4	10.10	5.23	3.49	4.10	N/A	3.41	N/A
	2.76	23.5	9.65	5.53	3.50	4.25	N/A	3.81	N/A
Average, θ (°)	N/A	N/A	9.27	4.74	3.62	4.23	N/A	3.49	N/A
Sheet Break-up Distance, $2r_{bu}/D_o$	0.69	11.8	49.43	37.58	37.11	30.56	N/A	21.48	N/A
	1.38	16.6	39.18	31.91	33.81	29.27	N/A	17.62	N/A
	2.07	20.4	37.39	30.72	N/A	27.31	N/A	15.30	N/A
	2.76	23.5	34.64	28.72	N/A	25.87	N/A	13.46	N/A
Overall Characteristic Drop Size, d_{v50}/D_o	0.69	11.8	0.155	0.091	0.085	0.101	0.104	0.087	0.056
	1.38	16.6	0.149	0.081	0.076	0.097	0.100	0.073	0.053
	2.07	20.4	0.143	0.082	0.080	0.094	0.103	0.062	0.048
	2.76	23.5	0.146	0.081	0.074	0.089	0.101	0.059	0.045

3.2.1 Sheet Formation

Due to viscous stress, the average sheet velocity decreased along the deflector. From conservation of mass, the sheet is thicker than that of an inviscid radially expanding film. A dimensionless sheet thickness which is defined by Eq. (2-8) will be used to describe the thickening effect of the sheet along the deflector. It should be noted that the thickness of the sheet may also increases from a hydraulic jump occurring on the shallow liquid layer [28]. However, calculations reveal that hydraulic jumps are not likely to occur on the deflector under normal operating conditions, but may occur at radial locations well beyond the deflector boundary.

Figure 7 provides a general view of the effect of geometry on the sheet thickness. The sheet thickness at the edge of the deflector is provided for a range of deflector geometries, D^*, and injection condition, Re. In Region II, the boundary layer
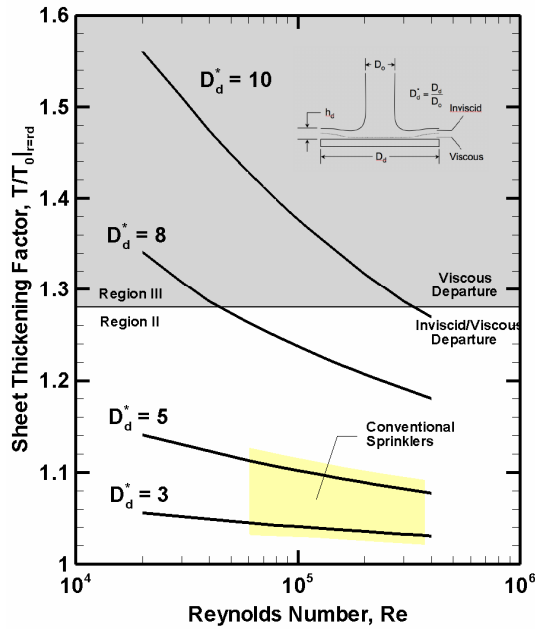

Figure 7. Sheet thickening factor

33

thickness is smaller than the sheet thickness and the sheet will be less affected by the deflector. However, in Region III, the boundary layer overwhelms the entire sheet. In this study, the dimensionless deflector diameters are 10.9, 5.7, and 3.9 for the basis nozzles. The large D^* configuration (small jets) will produce substantial sheet thickening at low Re. However, typical sprinkler operating conditions shown in Figure 7 corresponding to moderate Re and relatively small D^*. These conditions typically result in small viscous effect with $(T - T_0)/T_0 \mid_{r=r_d} < 15\%$.

3.2.2 Sheet Trajectory

Because of the forces within the sheet, the sheet trajectory is complex and different from trajectories of free shooting objects. Figure 8 shows an example of the sheet trajectory curve with the initial sheet velocity of 2 m/s, initial sheet thickness of 0.5 mm and initial sheet angle of 0º. Initially, the sheet is relatively straight which is similar to the trajectory of a discrete object (i.e. droplet). As the sheet expands, the sheet thickness becomes smaller. And the surface tension force increases rapidly, causing the curvature to increase and the sheet to bend. This kind of behavior can be observed when the working pressure is low. Theoretically, even at high pressures the sheet would bend similarly. However, it breaks up before reaching this point.

For canonical fire suppression nozzles, the sheet break-up distance is very small, and the trajectory is almost a straight line. Figure 9(a) shows the measurement of trajectory for the medium basis nozzle at 2.07 bar. Figure 9(b) shows the comparison of the experiment and simulation. It should be noted that the initial angle is
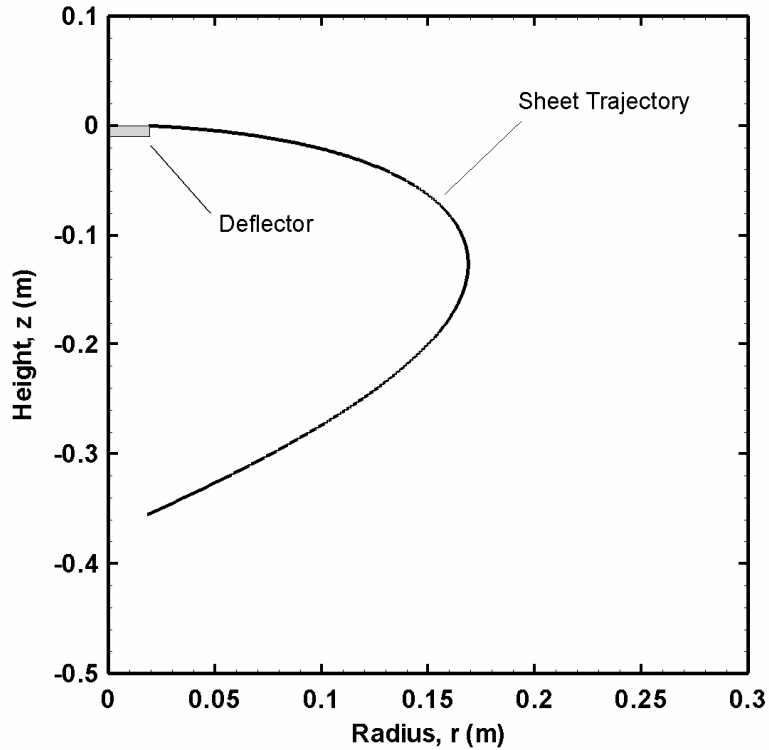
Figure 8. Sheet Trajectory Characteristics, U_{init} *= 2 m/s,* T_{init} *= 0.5 mm,*
θ_{init} *= 0°*

determined experimentally as an input to the trajectory model as discussed in
the approach.

The initial conditions required for the trajectory sub-model have been
presented in Figure 5 and Appendix A. These initial conditions were obtained
from other sub-models with the exception of the initial angle θ_{ini} . Because the
deflector is horizontal, θ_{ini} should be 0°. Figure 9(b) shows that the sheet initial
angle is small. However, θ_{ini} is critical to the dispersion analysis and the initial
drop size. Although models to predict θ_{ini} have not been developed yet; these
angles can be determined form PLIF tests [24]. Figure 10 provides a summary
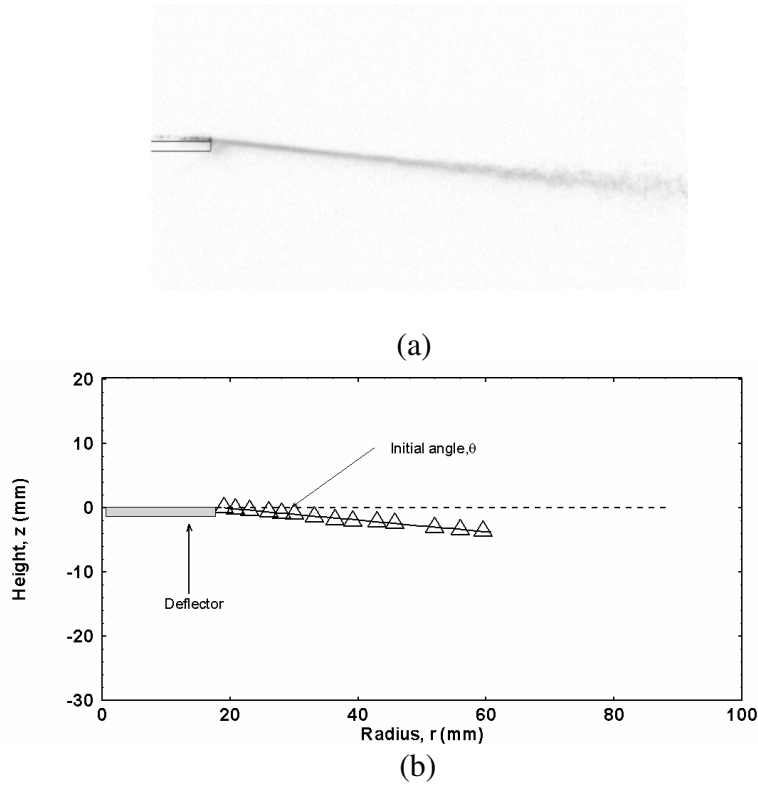
(a)

(b)

Figure 9. (a) Photograph of the sheet trajectory, K = 26.1 Lmin^{-1}bar$^{-1/2}$, *P = 2.07* bar*; (b) Comparison between experimental and modeled sheet trajectory, △ Measurement, ——— Model Prediction.*

of measured θ_{ini} for basis nozzles, the tined nozzle at the tine and standard nozzles at the tine. Unfortunately, the initial angle at the space of the tined and standard nozzles could not be measured due to the limitation associated with the PLIF measurement technique. The initial angle seems to be generally a function of sprinkler configuration, although the scatter at various *We* cannot be ignored (or explained).

Possible factors governing θ_{ini} could be

1.   Deflector surface effects

When the thin sheet leaves the deflector, it experiences a surface tension force attracting it towards the outside edge of the deflector, bending the sheet downward with an angle.
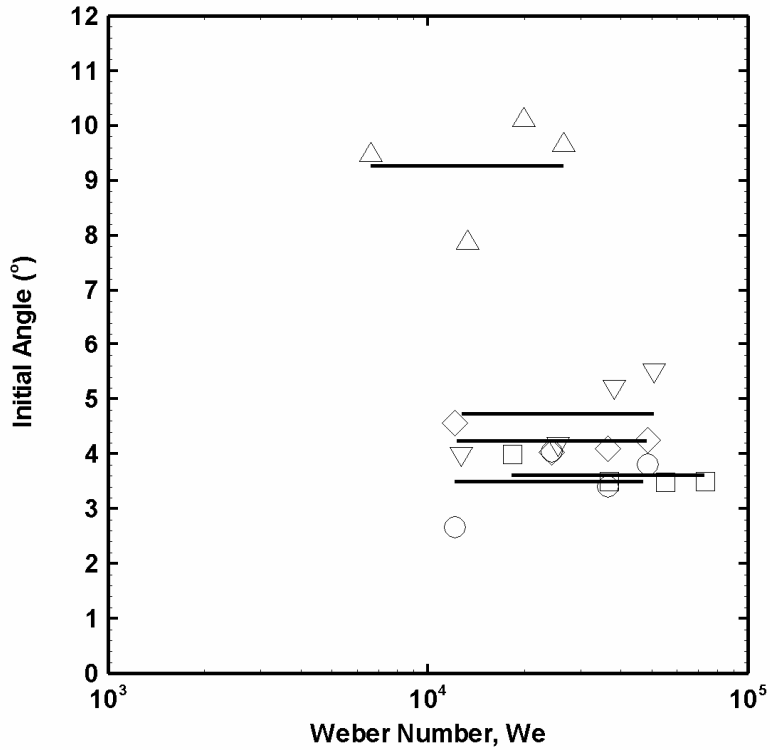
36

Figure 10. Sheet initial angle: ⎯⎯⎯*Average; Basis Nozzle* △ *D_0 = 3.5 mm,* ▽ *D_0 = 6.7 mm,* □ *D_0 = 9.7 mm; Tined Nozzle* ◇ *D_0 = 6.35 mm; Standard nozzle* O *D_0 = 6.35 mm*

2. Sheet Profile effects

The sheet thickness decreases along the deflector during its radial expansion producing a vertical velocity component. Without the vertical support of deflector, the sheet will travel downwards and the angle introduced here can be estimated from Eq. (3-3).

$$T \approx \frac{T_d r_d}{r} \tag{3-1}$$

$$\frac{dT}{dr} = -\frac{T_d r_d}{r^2} \tag{3-2}$$

$$\theta \approx \tan\theta = \frac{U_z}{U_r} = \frac{dT/dt}{dr/dt} = \frac{dT}{dr} = -\frac{T_d r_d}{r^2}\Big|_{r=r_d} = -\frac{T_d}{r_d} \qquad (3\text{-}3)$$

For the basis nozzle, θ will be approximately 1.5°, however, the contribution of the sheet profile effect seems only about one-third of the total measured initial angle. The remainder of the deflection may be attributed to the deflector surface forces. In fact the smallest nozzle producing the thinnest sheet is most easily influenced by the deflector surface forces and has an average initial angle of ~9°, over twice that the other nozzles.

PLIF images taken in planes orthogonal to a reference tine at radial locations of 12.7 mm, 22.7 mm and 62.7 mm are provided in Figure 11 and reveal an even more complex view of trajectory behavior in tined and basis nozzles. The trajectory appears to be initially affected by the spaces in the tined nozzle (22.7 mm). But this effect is overwhelmed by surface tension forces which keep the sheet intact as the sheet expands (62.7 mm). The standard nozzle shows a radially expanding sheet similar to
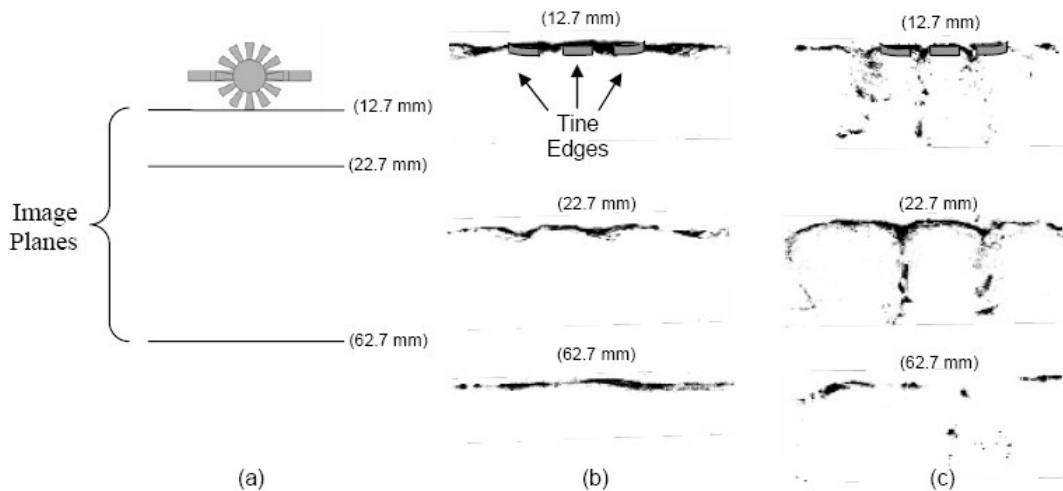

Figure 11. Inverted PLIF images depicting flow through sprinkler spaces; (a) Top view of measurement locations; (b) Tined nozzle; (c) Standard nozzle [24]

the other nozzles, but the boss directs flow through the spaces which is apparent at 12.7 mm and 22.7 mm. It is unknown how much fluid is directed through the space and if an orthogonal continuous liquid sheet is formed. Improved diagnostics should reveal a clearer view of atomization in this region.

3.2.3 Sheet Break-up and Drop Formation

Sheet break-up resulted from a flapping flag-like instability for all nozzle configurations and experimental conditions tested in this study. This mode of instability has been observed by other researchers in similar configurations, most notably Dombrowski [8], Huang [15] and Villermaux [17]. A photograph of flapping sheet break-up is shown in Figure 12. In the past, Huang's impinging jet experiments indicated two lower Weber number break-up regimes in addition to the flapping break-up regime occurring at $We > 2,000$. In the flapping regime, Huang observed clearly visible waves growing on the sheet before break-up. He also observed that the sheet break-up follows a $We^{-1/3}$ power law unlike the lower Weber number regime which follows a We^1 power law. The sheet break-up power law ($We^{-1/3}$) behavior associated with the flapping regime was also observed in this study. However, two break-up modes were observed in the high Weber number flapping regime, which categorized as the rim break-up and ligament break-up mode as shown in Figure 13.

Rim break-up mode

In this mode, the sheet breaks up into droplets as shown in Figure 13 (a). Waves
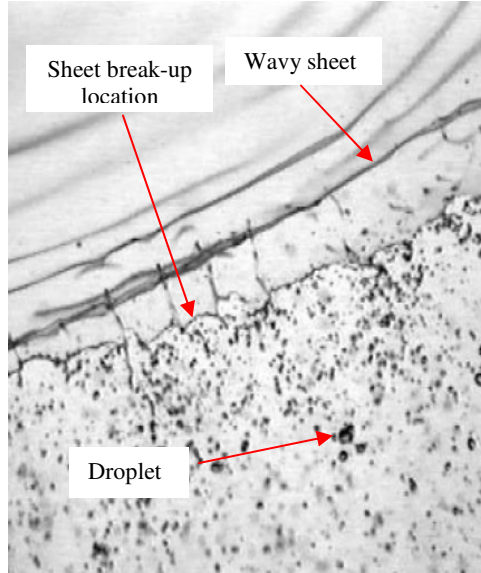
Figure 12. Snapshots of break-up of liquid sheet from Villermaux [17]

can be clearly observed on the sheet. The wave amplitude is growing as the sheet

expands radially outward. Previous analysis (§ 2.1.3) suggests that sheet break-up

into ligaments occurs when the amplitude reaches a critical value [8]. Although

critical amplitude approach is valid, an alternative break-up description based on *We*

arguments near the edge of the sheet is provided for the current analysis. A force

balance at the edge of the sheet is illustrated in Figure 14 and given by

$$\frac{F_I}{F_\sigma}\big|_{break-up} \sim \frac{\rho_l aT\lambda l}{2\sigma l}, \tag{3-4}$$
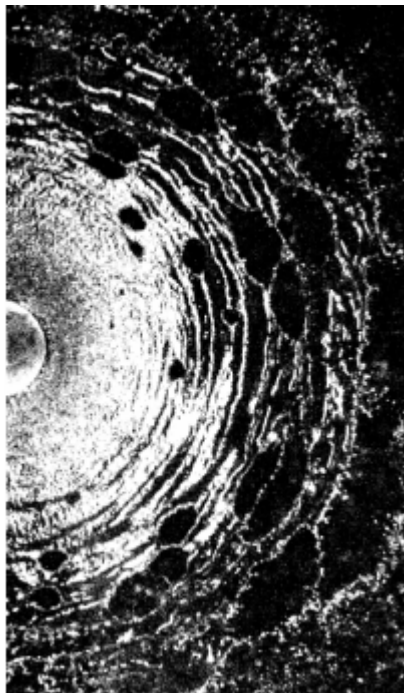
where a is the local maximum acceleration at the break-up location. The inertial

force tends to tear the sheet apart, while the surface tension force tends to keep the

sheet intact. Villermaux [17] suggests that
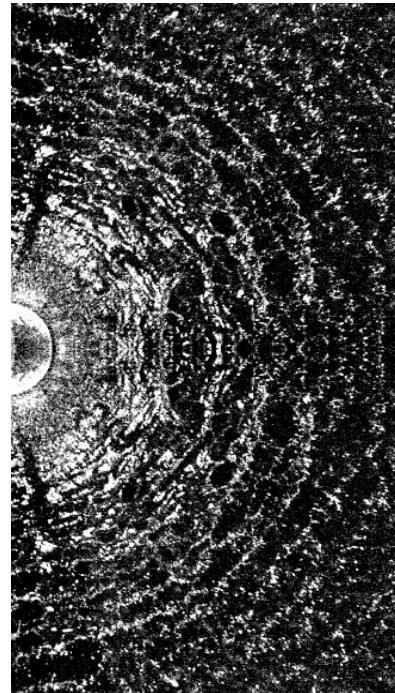
$$a = \frac{U^2}{\lambda}\rho^{*1/3}, \tag{3-5}$$

yielding

40

Figure 13. (a) Rim break-up mode; (b) Holes generated in rim break-up mode; (c) Ligament break-up mode.

$$\frac{F_I}{F_\sigma}\Big|_{break-up} \sim \frac{\rho U^2 T}{2\sigma} = \frac{\rho^{*1/3} We_{sheet}}{2} . \qquad (3\text{-}6)$$

The sheet Weber number at the break-up location is not intended to provide a critical condition for sheet break-up. This condition is provided by the critical amplitude. On the contrary, the Weber number at the break-up location is intended to describe the condition at the edge of the sheet which is expected to be important for describing the mode of fragmentation and drop formation at the edge of the sheet. Experiment photographs, Figure 14, show that rim break-up mode occurs when $We_{sheet} < 150$.

Holes

As *We* increases, holes are generated on the sheet. These holes expand due to surface tension and may affect sheet break-up and drop formation. Holes can be generated from satellite droplets impacting on the sheet or from extreme large fluctuations in amplitude possibly caused by an upstream event. These holes begin to occur at $We_{sheet} > 50$ while the flapping sheet is still in the rim break-up mode and continue to be observed in the ligament break-up mode.
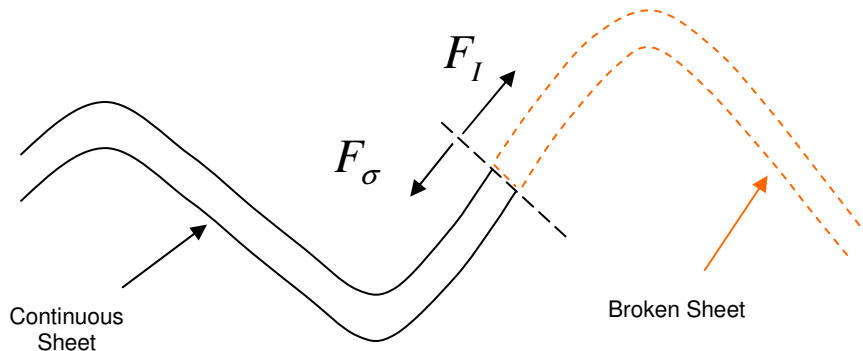

Figure 14. Force dynamic at the rim of sheet

Ligament break-up mode

When $We_{sheet} > 150$, the sheet breaks up in the ligament break-up mode. In this mode, the sheet will not break-up into droplets directly. First, it breaks up into ring-like ligaments as shown in Figure 13(c) and described in §2.2.3. These ligaments break up into droplets. The atomization model in this study is formulated based on the ligament break-up mode. The nozzle configuration and operating pressures for fire suppression nozzles are expected to produce $We_{sheet} > 150$. These nozzles should produce flapping sheets that form droplets in the ligament mode. More measurements are required to confirm this assertion, especially in complex geometries.

The added geometrical features of the standard nozzles produce an even more complex sheet structure than the basis nozzle. Due to the presence of tines and the boss, the sheet formation model is no longer valid. The sheet surface interactions are different between the flow through the boss and tine and the flow through the space. The boss directs the flow through the spaces creating distinct radially expanding sheets along the tine, and boss oriented streams in the space as shown in Figure 15.

The current atomization modeling shortcomings for evaluating actual fire suppression nozzles have been revealed in the previous discussion. Although the potential for sheet break-up in the rim model is not likely for typical nozzle operating conditions and geometries ($We_{sheet} > 150$), the presence of holes in the sheet and the complicated sheet structure owing to the tines, spaces, and boss will require additional treatment. The importance of these effects will become evident from analysis of the data.
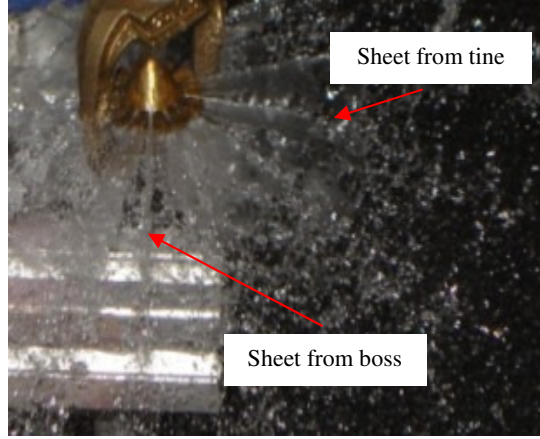
Figure 15. Sheet formation from tine and boss for standard nozzle

3.3 Scaling Law Evaluation

The scaling law for sheet break-up location and drop size are based on Dombrowski's analysis [8, 26] presented in §2.3. Assuming an inviscid unstable sheet and a ligament sheet break-up mode. Eq. (2-37) shows that the sheet break-up location is not only a function of *We*, but also related to the initial sheet thickness, deflector diameter, initial sheet angle, air liquid density ratio and critical dimensionless amplitude at break-up. A convenient sheet break-up parameter including these effects is defined as $X_{sheet} = \dfrac{3 f_0 \cos\theta_{ini}}{2\rho^* r_d^*}\left(\dfrac{2 T_d^* \beta^2}{We}\right)^{\frac{1}{2}}$. Figure 16(b) shows the break-up data in terms of the break-up parameter. The dimensionless amplitude f_0 has been adjusted to fit the theory for each nozzle according to Table 2.
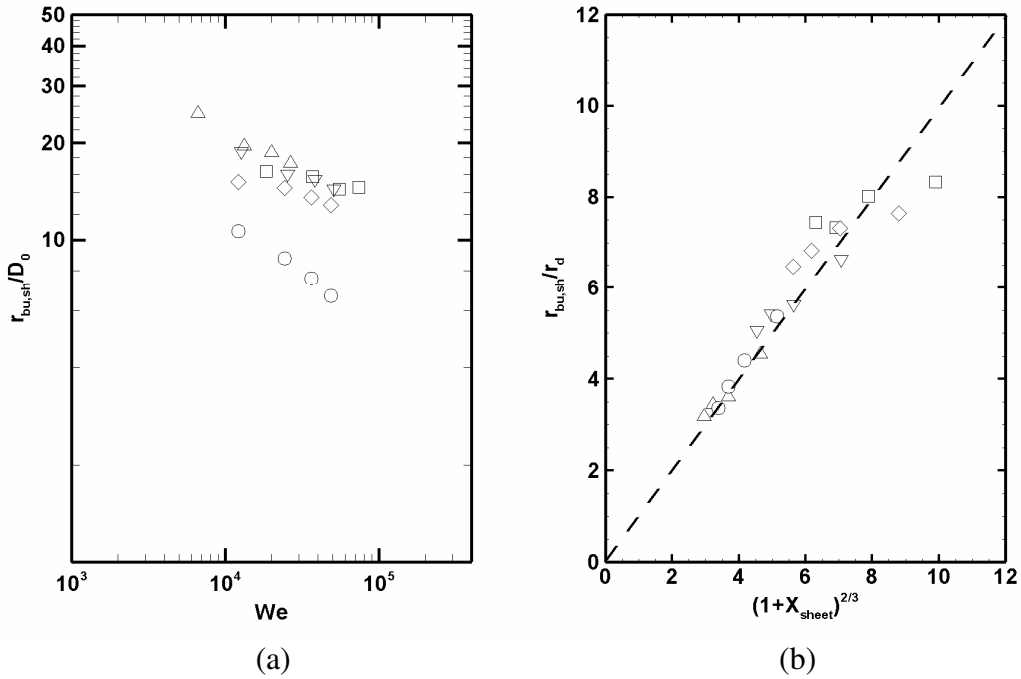
Figure 16. Experimental sheet break-up results: (a) Basis Nozzle △ D_0 = 3.5 mm, Tined Nozzle ▽ D_0 = 6.7 mm, Standard Sprinkler □ D_0 = 9.7 mm, ◇ D_0 = 6.35 mm, O D_0 = 6.35 mm; (b)— — — scaling law.

For the basis nozzle, this change in f_0 may be related to changes in the initial disturbance characteristics associated with the different nozzle size. For the standard nozzle, the flow through the spaces may have reduced T_d^*. Because this effect is not

Table 2. Critical dimensionless wave amplitude

Nozzle	f_0
Basis Nozzle (Small, $D_0 = 3.5mm$)	7.13
Basis Nozzle (Medium, $D_0 = 6.7mm$)	13.33
Basis Nozzle (Large, $D_0 = 9.7mm$)	18.13
Tined Nozzle ($D_0 = 6.35mm$)	10.13
Standard Nozzle ($D_0 = 6.35mm$)	3.95

taken into account, the adjusted f_0 may be set too low having to compensate for the relatively large T_d^* used in the calculations. Nevertheless, the sheet break-up location reduces with increasing We. In fact, for $X \gg 1$, which is the case for most of the measurements Eq. (2-37) simplifies to Eq. (2-38), and $r_{bu,sh}^* / r_d^* \sim We^{-1/3}$.

Similar to the sheet break-up analysis, drop size scaling law in Eq. (2-34) shows that drop size is a strong function of nozzle size and configuration. A characteristic drop size is typically reported for a spray based on an averaging scheme or based on some measure of a particular feature of the drop size distribution [48]. In this study, the d_{v50} or volume median diameter is used. Fifty-percent of the spray volume is contained in drop sizes smaller (or larger) than the d_{v50}. Ideally, the drop size calculated from the measured distribution is expected to follow the trends determined from the deterministic analysis. However, the magnitude of the characteristic drop size may differ from the deterministic values. In fact, in this study, the stochastic model predicts a $d_{v50} \approx 1.3d$, where d is the deterministically calculated drop size. A similar approach of determining a correlation factor to relate the d_{v50} to deterministic value was also used by Dombrowski [8]. Eq. (2-44) can be modified based on this factor to estimate a scaling law for d_{v50} yielding

$$d^* = 4.5(\rho^*)^{-1/6}\left(\cos^{1/2}\theta_{ini}\frac{r_d^* T_d^* \beta^2}{f_0}\right)^{1/3}(We)^{-1/3} = X_{drop}. \qquad (3\text{-}7)$$

According to Eq. (3-7), the dimensionless drop size should follow a $We^{-1/3}$ power law. Furthermore the coefficients are given by the density ratio, and parameters related to the nozzle configuration. Figure 17(a) shows basis nozzle drop size dependence with We, which is much weaker ($\sim We^{-1/6}$ power law) than the theoretical

$We^{-1/3}$ behavior. The data, however, does suggest a configuration dependent coefficient related to this unexpected weaker power law. Figure 17(b) shows the data compared directly against the scaling law in Eq. (3-7). For the basis nozzle, higher We (lower X_{drop}) data tend to provide better agreement with the theory. Previously in Figure 13, it was suggested that the sheet break-up mode was determined by the sheet Weber number at the break-up location and this parameter influenced the drop formation behavior. Rim break-up mode and ligament break-up mode were observed in our experiments; however, the scaling laws are based on ligament break-up mode assumptions. The discrepancy between the scaling law and measured drop sizes suggests that little of the measurements were taken in ligament mode. Figure 18(a) shows only data where $We_{sheet} > 150$ (ligament break-up mode)

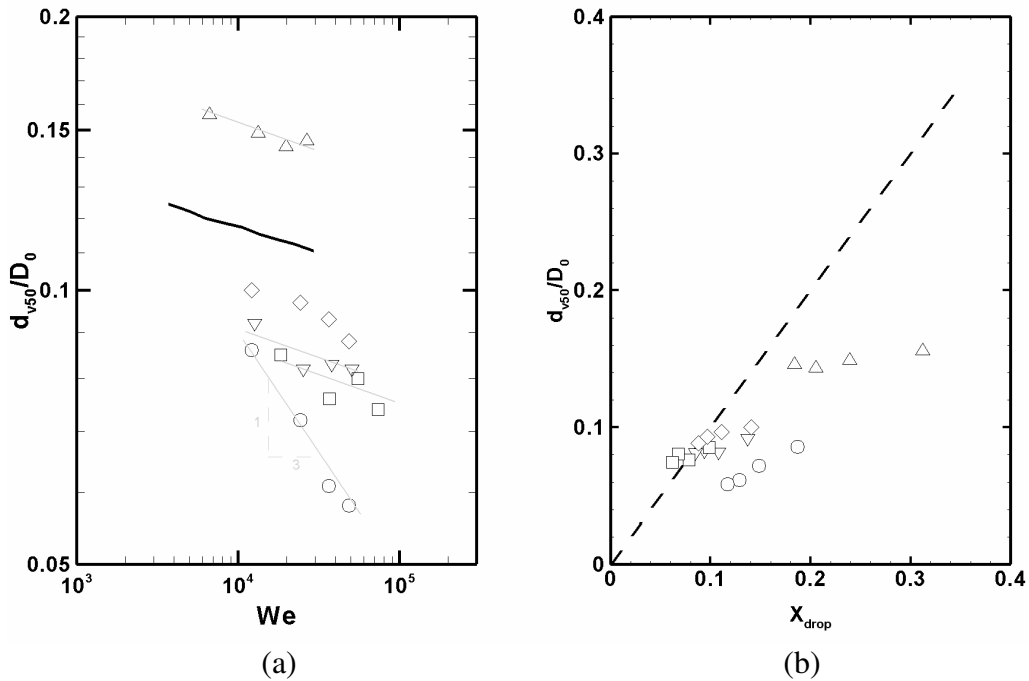(a)   (b)

Figure 17. Experimental drop size and scaling law: (a) ──── Villermaux; Basis Nozzle △ $D_0 = 3.5$ mm, ▽ $D_0 = 6.7$ mm, □ $D_0 = 9.7$ mm, ◇ $D_0 = 6.35$ mm, O $D_0 = 6.35$ mm; (b)── ── ──stochastic model prediction.

The agreement with the scaling law is occur, although the data is limited. More experiments, perhaps with bigger nozzles at higher pressures will increase the data in this mode. Figure 18(b) also shows that the scaling law errors become relatively small in ligament break-up mode where the agreement with the scaling law is clear. The error is defined as

$$error = \frac{\left| D_{v50\_Pr\,edicted} - D_{v50\_Measured} \right|}{D_{v50\_Measured}} \times 100\% . \qquad (3\text{-}8)$$

The standard nozzle displays a very different drop size behavior from the basis nozzles. A clear $We^{-1/3}$ power law behavior is observed in Figure 17(a). Although the standard nozzle drop size trend follows the theory, the measured drop sizes are much smaller than those predicted by the scaling laws. This

(a)   (b)
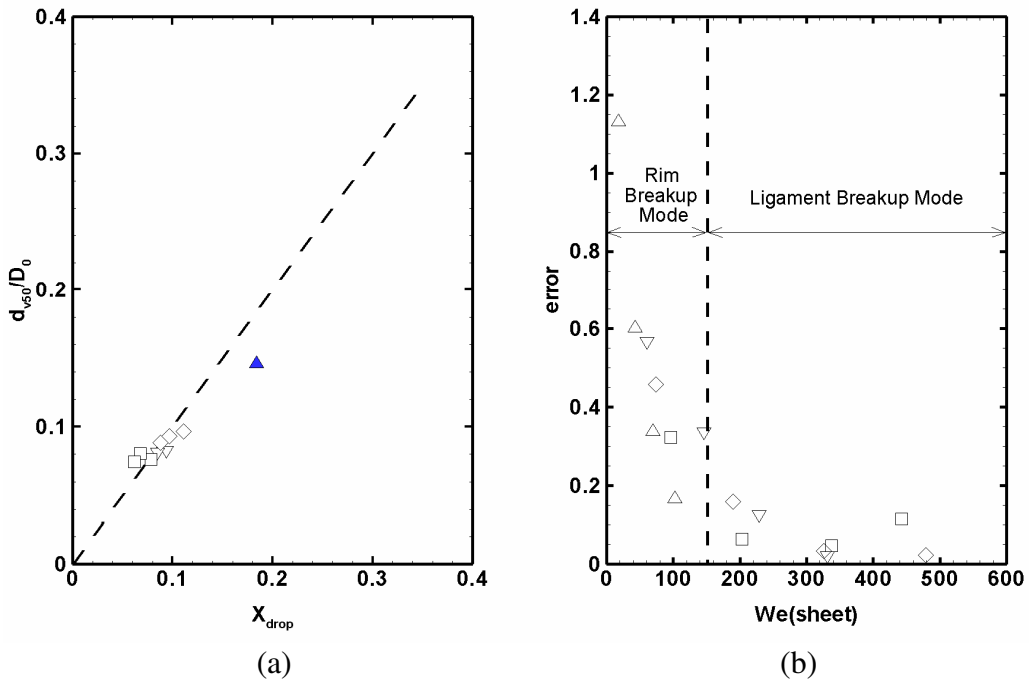
Figure 18. Dimensionless drop size: (a)Drop size in ligament break-up mode, Basis Nozzle △ D_0 = 3.5 mm, ▽ D_0 = 6.7 mm, □ D_0 = 9.7 mm, Tined Nozzle ◇ D_0 = 6.35 mm; (d) error as a function of sheet Weber number at break-up location.

discrepancy may be related to the large sheet thickness estimated in the scaling law which does not account for the mass loss through the spaces and the associated small value of f_0. Both of these discrepancies will cause the data to shift away from the theory. More experiments and nozzle configurations are needed to measure the sheet thickness to better apply the theory to actual nozzles.

Chapter 4: Summary and Conclusions

A physics based atomization model to predict characteristics of the initial spray has been modified and evaluated through comparisons with canonical fire suppression nozzles of varying complexity. A trajectory model has been implemented and experimental observations have been critically examined to evaluate the validity of the basic modeling assumptions and physics. The model was evaluated quantitatively by comparing measurements with scaling laws obtained from model equations. The main conclusions from this analysis are summarized below.

Sheet formation: Analysis shows that the sheet thins as it expands radially; however, viscous interaction with the deflector results in sheets that are thicker and slower than those obtained from simple inviscid analysis.

Trajectory: The trajectory model agreed well with measurements (showing a nearly constant trajectory angle), but required specification of the measured starting angle at the edge of the deflector. This starting angle is determined by the rate of thinning of the sheet and surface tension effects at the deflector edge, not accounted for in the model.

Sheet Break-up: Flapping sheet break-up was observed for all measurements. The sheet break-up location followed the scaling laws based on the model theory demonstrating a $We^{-1/3}$ power law behavior.

Drop Formation: The sheet breaks up directly into droplets in rim break-up mode ($We_{sheet} < 150$), but breaks up into ligaments and then drops in ligament break-up mode ($We_{sheet} > 150$), consistent with modeling assumptions. The model and

associated scaling laws agree with measurement when the sheet breaks up in ligament mode although limited data at the higher operating pressure and jet diameters associated with this mode. Additional ligament mode measurement will be performed in future work.

Sprinklers: Evaluation of the standard nozzle with its complex sprinkler-like geometry provides insight into sprinkler behavior. Scaling law trends for the sheet break-up location and drop size following $We^{-1/3}$ were observed. However, the magnitude of the dimensionless drop size was much smaller than that predicted by the scaling laws, perhaps due to sheet thinning effects owing to flow bias in the spaces not accounted for in the scaling laws. This effect will be explored in future work.

Appendices

Appendix A: Model Input and Formulations

Sheet Formation Model

The object of sheet formation model is to determine the sheet thickness and velocity at the edge of deflector, which is the input of trajectory model. The input quantities include

$$P,\ \rho_l,\ \rho_a,\ K,\ D_d.$$

And the output quantities include

$$U_{sheet},\ T_d,\ r_d.$$

Table A.1 is the summary of all the quantities and the variable names used in the sheet formation sub-model

Table A.1. Summary of variables in sheet formation model

Symbol	Physical meaning	Corresponding parameter in code
P	Pressure	*pressure*
ρ_l	Density of liquid	*rol*
ρ_a	Density of air	*roa*
μ_l	Kinetic viscosity of the liquid	*miul*
K	K-factor of the nozzle	*kfactor*
D_0	Diameter of deflector	*D0*
r_d	Radius of the deflector	*rad*
U	Jet velocity	*ujet*
U_{sheet}	Velocity of the sheet at the deflector edge	*usheet*
Q	Flow rate of the nozzle(Kg/s)	*qflow*
r_o	Radius of the jet	*rjet*
r_1	Boundary layer region	*roturb*
T_d	Film thickness at the deflector edge	*thdef*
l	An arbitrary constant length	*lcharturb*

The following is the list of equations that used in the sheet formation sub-model

$$U = \left(\frac{2P}{\rho_l}\right)^{1/2}$$

$$r_o = \left(\frac{K}{\pi}\right)^{1/2}\left(\frac{\rho_l}{2}\right)^{1/4}$$

$$Q = KP^{1/2}$$

$$T_d = \begin{cases} \dfrac{r_o}{2r_d} + 0.01659 \times \left(\dfrac{7v_l}{U_o}\right)^{1/5} r_d^{4/5} & r_d < r_1 \\[3ex] 0.0211 \times \left(\dfrac{v_l}{Q}\right)^{1/4} \dfrac{r_d^{9/4} + l^{9/4}}{r_d} & r_d > r_1 \end{cases}$$

$$l = 4.126 \times r_o \left(\frac{Q}{v_l r_o}\right)^{1/9}$$

$$U_{sheet} = \frac{Q}{2\pi r_d h_d}$$

Sheet Trajectory Model

The object of sheet trajectory model is to calculate the sheet thickness and velocity as the sheet expands outwards, which will be used in wave dispersion model. The input quantities include

$$U_0,\ z_0,\ T_d,\ r_d,\ \theta_0,\ U_a,\ \Delta p_g.$$

And the output quantities include

$$U,\ T,\ r,\ z,\ \theta,\ \xi.$$

Table A.2 is the summary of all the quantities and the variable names used in the trajectory sub-model

Table A.2. Summary of variables in trajectory model

Symbol	Physical meaning	Corresponding parameter in code
U_{sheet}	Initial velocity of the sheet	*usheet*
Z_0	Initial vertical position of the sheet	*(assume 0 in the code)*
θ_0	Initial angle of the trajectory	*an*
U_a	Velocity of the air	*(assume 0 in the code)*
Δp_g	Pressure difference between the sheet	*(assume 0 in the code)*
U	Sheet velocity	*traj(i).v*
z	Vertical position of the sheet	*traj(i).z*
r	Radius position of the sheet	*traj(i).r*
T	Thickness of the sheet	*traj(i).thick*
θ	Trajectory angle(between the tangent of the trajectory and horizontal line)	*traj(i).angle*
ξ	Natural axis along the sheet	*traj(i).s*
μ_a	Dynamic viscosity of the air	*miua*
Re	Reynolds number based on the diameter of the deflector	*Re*
S	Gas-liquid interfacial friction factor	*s0*
g	Gravity	*9.8m/s²*

The following is the list of equations used in the trajectory sub-model

$$S = -\frac{\rho_a}{2T}[0.79(1+150T/r)\,\mathrm{Re}^{-1/4}](U_a - U)^2$$

$$\mathrm{Re} = \frac{2\rho_a r_d}{\mu_a}|U_a - U|$$

$$\begin{cases} rT\dfrac{dU}{d\xi} + UT\dfrac{dr}{d\xi} + Ur\dfrac{dT}{d\xi} = 0 \\[2mm] \rho_l U\dfrac{dU}{d\xi} = S + \rho_l g\cos\theta \\[2mm] \rho_l U^2\dfrac{d\theta}{d\xi} = -\dfrac{\Delta p_g}{T} - \dfrac{2\sigma}{T}\left(\dfrac{\cos\theta}{r} - \dfrac{d\theta}{d\xi}\right) - \rho_l g\sin\theta \\[2mm] \dfrac{dr}{d\xi} = \sin\theta \\[2mm] \dfrac{dz}{d\xi} = \cos\theta \end{cases}$$

Wave Dispersion Model

The object of wave dispersion model is to calculate the wave growth rate and determine where the sheet breaks up, which will be used in ligament break-up model. The input quantities include

$$U, T, r, z, \theta, \xi.$$

And the output quantities include

$$f, n_{crit,sh}, \lambda_{crit,sh}.$$

Table A.3 is the summary of all the quantities and the variable names used in the wave dispersion sub-model.

Table A.3. Summary of variables in wave dispersion model

Symbol	Physical meaning	Corresponding parameter in code
f	Dimensionless amplitude	f0
n	Wave number	x1, x2
$\lambda_{crit,sh}$	Critical wavelength	Sheet(i).lambda
$n_{crit,sh}$	Critical wave number	sheet(i).ncrit
d_{lig}	Ligment diameter	lig(i).diameter
m_{lig}	Ligment mass	lig(i).mass
$r_{bu,sh}$	Radius location of sheet break-up	sheet(i).rbreak, lig(i).r1
$T_{bu,sh}$	Film thickness at break-up	sheet(i).thick

The following is the list of equations used in the wave dispersion sub-model

$$\left(\frac{\partial f}{\partial t}\right)^2 + \frac{\mu_l}{\rho_l}n^2\left(\frac{\partial f}{\partial t}\right) - \frac{2(\rho_a nU^2 - \sigma n^2)}{\rho_l T} = 0$$

$$\left(\frac{\partial f}{\partial t}\right)^2 - \frac{2(\rho_a nU^2 - \sigma n^2)}{\rho_l T} = 0$$

$$m_{lig} = \pi\rho_l h_{bu,sh}[(r_{bu,sh} + \pi/n_{crit,sh})2 - r^2{}_{bu,sh}]$$

$$m_{lig} = \pi^2\rho_l\frac{d^2{}_{lig}}{2}\left(r_{bu,sh} + \frac{d_{lig}}{2}\right)$$

Ligament break-up model

The object of ligament break-up model is to determine the drop size distribution and initial drop location. The input quantities include

$$d_{lig}, \ U, \ r_{bu,sh.}$$

And the output quantities include

$$d, \ r_{drop}, \ U_{drop}.$$

Table A.4 is the summary of all the quantities and the variable names used in the ligament break-up.

Table A.4. Summary of variables in ligament break-up model

Symbol	Physical meaning	Corresponding parameter in code
U_{drop}	Critical wave number	n
$\lambda_{crit,lig}$	Critical wavelength for ligament break-up	$lig(i).wavelength$
$t_{bu,lig}$	Ligament break-up time	$lig(i).time$
r_{drop}	Initial drop loction	$lig(i).r2, \ drop(i).r1$
d	Drop diameter	$drop(i).diameter$

The following is the list of equations used in the ligament break-up sub-model

$$nd_{lig} = \left[\frac{1}{2} + \frac{3\mu_l}{2(\rho_l d_{lig}\sigma)^{1/2}} \right]^{1/2}$$

$$d = d_{lig}^{2/3} \left(\frac{3\lambda_{crit,lig}}{2} \right)^{1/3}$$

$$t_{bu,lig} = 24 \left(\frac{2\rho_l}{\sigma} \right)^{1/2} \left(\frac{d_{lig}}{2} \right)^{3/2}$$

Appendix B: Description of Stochastic Model

In the deterministic model, the critical dimensionless break-up amplitude f is assumed to be a constant. However, this critical condition may vary with the largely unknown distribution of initial disturbance amplitudes as shown in Figure 6. We can see clearly that the surface of jet is not smooth at all. Waves appear on both of the jet and the film on the deflector. In the wave dispersion model, the dimensionless wave amplitude is defined as $f = \ln(A/A_0)$. However, the initial wave amplitude A_0 is unknown and can change the critical dimensionless amplitude. In the stochastic model, the dimensionless critical sheet break-up amplitude is treated as a discrete random variable $f[m]$ defined over an m-element space to account for the assumed distribution of initial disturbances. This amplitude ratio $f[m]$ satisfies a normal distribution specified by the mean critical sheet break-up amplitude, $\bar{f} = 12$ and the fluctuation intensity, I_f. This fluctuation intensity is a modeling parameter defined as

$$I_f = \frac{\sigma_f}{\bar{f}}.$$

where σ_f is the standard deviation of $f[m]$. The random variable $f[m]$ is used in the wave dispersion model resulting in m different critical sheet break-up wavelengths, sheet break-up times, and sheet break-up locations. These distributed parameters will influence thee subsequent ligament formation and break-up analysis.
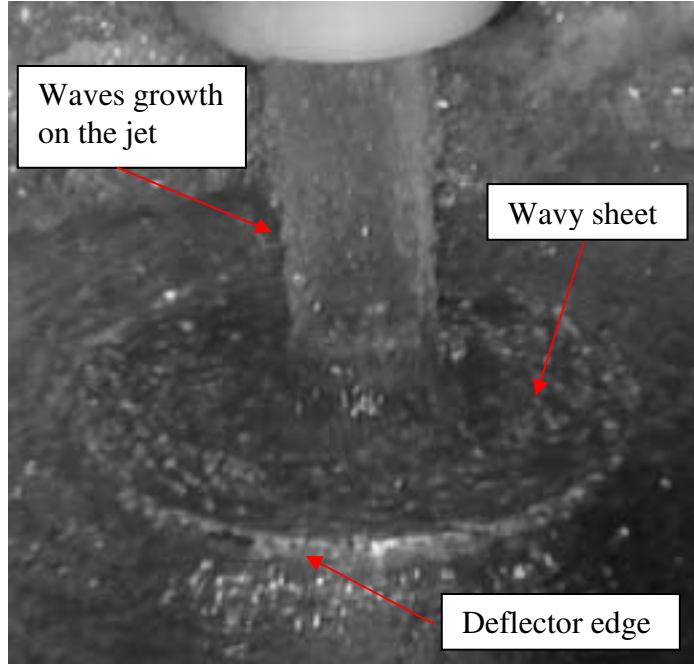
Figure B.1. Initial disturbance on the jet

In the sheet break-up model, the sheet is assumed to break up into ring-like structures having radial width of one-half wavelength. These ring-like structures rapidly contract into torroidal ligaments, which in turn break up into drops. The sheet, of course, does not always break up into one-half wavelength fragments. In the stochastic model, the radial width of the ligament fragments, $\Delta r_{lig}[m,n]$, is treated as a discrete random variable based on a chi-square distribution defined for each sheet break-up realizations. The chi-square distribution prevents the occurrence of negative fragment widths at high fluctuation intensities. The specified sheet break-up fluctuation intensity is defined as

$$I_{lig} = \frac{\sigma_{lig}[m]}{\Delta r_{lig}[m]}.$$

This intensity and the mean ligament fragment width ($\overline{\Delta r_{lig}[m]} = \overline{\lambda_{crit,lig}[m]/2}$) calculated from the model are used to determine the standard deviation of sheet

58

fragment widths $\sigma_{lig}[m]$. These quantities are used to define the chi-square distribution and the resulting ligament fragment widths, $\Delta r_{lig}[m,n]$.

Similarly, the ligament fragment widths, $\Delta w_{drop}[m,n,p]$, are given by a chi-square distribution. The specified fluctuation intensity,

$$I_{drop} = \frac{\sigma_{drop}[m,n]}{\Delta w_{drop}[m,n]},$$

and the mean ligament fragment width, $\overline{\Delta w_{drop}[m,n]} = \overline{\lambda_{crit,lig}[m,n]}$, defines this distribution. In all $m \times n \times p$ drop sizes are obtained in the stochastic model together with the number of drops at each of the possible drop sizes. In the current study, m, n, and p are specified as 1000, 50, and 50, respectively in order to obtain sufficient statistics for a smooth drop size distribution.

Guidance for I_f, I_{lig}, I_{drop} values have yet to be established from measurements. These parameters are expected to be influenced by the injector geometry and the injection pressure. Currently, these values can only be estimated until data or models are available to provide guidance on values for these parameters. Careful measurements are currently being conducted from experiments over a range of configurations and operating conditions to support continued development of the atomization model. Predictions have been shown to agree with measurements using parameter ranges $0.05 < I_f < 0.25$, $0.1 < I_{lig} < 0.3$, and $0.1 < I_{drop} < 0.3$ [45].

Bibliography

1. Rayleigh, On the Capillary Phenomena of Jets, *Proceedings of the Royal Society of London*, Vol. 29, 1879, pp. 71-97.

2. Weber, Z., *Angew Math Mech.*, Vol. 11, 1931, pp. 136-154.

3. Sterling, A. M., Sleicher, C.A., The instability of capillary jets, *Journal of Fluid Mech.*, Vol. 68, 1975, pp. 477-495

4. Squire, H. B., Investigation of the instability of a moving liquid film, British Journal of Applied Physics, Vol. 4, 1953, pp. 167-169

5. Hagerty, W. W., Shea, J. F., A study of stability of plane fluid sheets. J. Appl. Mech., Vol. 22, 1955, pp. 509-514.

6. Taylor, G., The Dynamics of Thin Sheets, of Fluid. III. Disintegration of Fluid Sheet, *Proc. R. Soc. Lond.*, Vol. 253. 1959, pp. 313-321.

7. Dombrowski, N., Hasson, D., Ward, D.E., Some aspect of liquid flow through fan spray nozzles, *Chemical Engineering Science*, Vol. 12, 1959, pp. 35-50.

8. Dombrowski, N., Hooper, P.C., The aerodynamic instability and disintegration of viscous liquid sheets, *Chemical Engineering Science*, Vol. 18, 1963, pp. 203-214.

9. Dombrowski, N., Johns, W.R., The effect of ambient density on drop formation in sprays, *Chemical Engineering Science*, Vol. 17, 1962, pp. 291-305.

10. Clark C. J., Dombrowski, N., Aerodynamic instability and disintegration of inviscid liquid sheets, *Proc. R. Soc. Lond.*, A. 329, 1972, pp. 467-478.

11. Crapper, G. D., Dombrowski, N., Pyott, G. A. D., Large amplitude Kelvin-Helmholtz waves on thin liquid sheets, *Proc. R. Soc. Lond.*, A. 342, 1975, pp. 290-224.

12. Li, X, Tankin, R.S., Droplet size distribution: A derivation of a Nukiyama-Tanasawa type distribution function, *Combust. Sci. and Tech.*, Vol. 56, 1987, pp. 65-76.

13. Li, X., Tankin, R.S., Derivation of drop size distribution in sprays by using information theory, *Combust. Sci. and Tech.*, Vol. 60, 1988, pp. 345-357.

14. Li, X., Tankin, R.S., On the temporal instability of a two-dimensional viscous liquid sheet, *Journal of Fluid Mech.*, Vol. 226, 1991, pp. 425-443.

15. Huang, J. C. P., The break-up of axisymmetric liquid sheets, *Journal of Fluid Mech.*, Vol. 43, 1970, pp. 305-319.

16. Clanet, C., Villermaux, E., Life of a smooth liquid sheet, *Journal of Fluid Mech.*, Vol. 462, 2002, pp. 307-340.

17. Villermaux, E., Clanet, C. Life of a flapping liquid sheet, *Journal of Fluid Mech.*, Vol. 462, 2002, pp. 341-363.

18. Dundas, P. H., Technical report optimization of sprinkler fire protection the scaling of sprinkler discharge: prediction of drop size, *Factory Mutual Research Corporation*, Norwood, MA, June 1974.

19. Heskestad, G., Proposal for studying Interaction of Water Sprays with Plume in Sprinkler Optimization Program, Memorandum to C. Yao, June 16, 1972.

20. You, H.Z., Investigation of spray patterns of selected sprinklers with the FMRC drop size measuring system, *First International Symposium on Fire Safety Science*, New York, pp. 1165-1176, 2986

21. Pilch, M., Erdman, C. A., Use of break-up time data and velocity history data to predict the maximum size of stable fragments for acceleration-induced break-up of liquid drop, *International journal of multiphase flow*, Vol. 13, 1987, pp. 741-757.

22. Widmann, J. F., Phase droppler interferometry measurements in water spray produced by residential fire sprinklers, Fire Safety Journal, Vol. 36, 2001, pp. 545-567

23. Sheppard, D. T., Spray characteristic of fire sprinkler, Nist GCR 02-838, *National Institute of Standards and Technology, Gaithersburg*, MD, 2002.

24. Blum, A., Marshall, A. W., *Discharge characteristics of canonical sprinkler sprays*, M.S. Thesis, University of Maryland-College Park, 2006.

25. Ibrahim, E.A., McKinney, T.R., Injection characteristics of non-swirling and swirling annual liquid sheets, *Jannaf Propulsion Conference*, Las Vegas, Nevada, May 10-13, 2004.

26. Wu, D., *Atomization model development for fire suppression devices*, M.S. Thesis, University of Maryland-College Park, 2005

27. Ren, N., Blum, A., Wu, D., Marshall, A., Characterizing the initial spray from fire suppression devices, *International Mechanical Engineering Congress and Exposition*, Chicago, Illinois, Nov. 5-10, 2006.

28. Watson, E. J., The radial spread of a liquid jet over a horizontal plane, *Journal of Fluid Mech.*, Vol. 20, 1964, pp. 481-499.

29. Vassallo, P., Ashgriz, N., Satellite formation and merging in liquid jet break-up, *Proc. R. Soc. Lond.*, A. 433, 1991, pp. 269-486.

30. Weihs, D., Stability of thin, radially moving liquid sheets, *Journal of Fluid Mech.*, Vol. 87, 1978, pp. 289-298.

31. Lin, S. P., Jiang, W.Y., *Absolute and convective instability of a radially expanding liquid sheet, Physics of Fluids*, Vol. 15, pp. 1745-1754.

32. Lin, S. P., Reitz, R. D., Drop and spray formation from a liquid jet, Annu. Rev. Fluid Mech., Vol. 30, 1998, pp. 85-105.

33. Walmsley, S.J., Yule, A.J., A study of the sprays produced by fire suppression system(bad), *Eighth International Conference on Liquid Atomization and Spray Systems*, CA, July 2000.

34. Prahl, J. M., Wendt, B., Discharge distribution performance for an axisymmetric model of a fire sprinkler head, *Fire Safety Journal*, Vol. 14, 1988, pp. 101-111.

35. Miesen, R., Boersam, B.J., Hydrodynamic stability of a sheared of a liquid film(Unread), *Journal of Fluid Mech.*, Vol. 301, 1995, pp. 175-202.

36. Koo, J. H., Kneer, M. J., Chaboki, A. C., Statistical Approach to Evaluate Particle Size Inversion Algorithms, *28th Aerospace Sciences Meeting*, Reno, Nevada, Jan. 8-11, 1990.

37. Babinsky, E., Sojka, P. E., Modeling drop size distributions, *Progress in Energy and Combustion Science*, Vol. 28, 2002, pp. 303-329.

38. Lasheras, J. C., Villermaux, E., Hopfinger, E. J., Break-up and atomization of a round water jet by a high-speed annular air jet, *Journal of Fluid Mech.*, Vol. 357, 1998, pp. 351-379.

39. Yoon, S. S., Kim, H. Y., Effect of Initial Conditions of Modeled PDFs on Droplet Characteristics for Coalescing and Evaporating Turbulent Water Spray Used in Fire Suppression Applications

40. Sallam, K. A., Dai, Z., Faeth, G. M., Drop formation at the surface of plane turbulent liquid jets in still gases, *International Journal of Multiphase Flow*, Vol. 25, 1999, pp. 1161-1180.

41. Sallam, K. A., Dai, Z., Faeth, G. M., Liquid break-up at the surface of turbulent round liquid jets in still gases, *International Journal of Multiphase Flow*, Vol. 28, 2002, pp. 427-449.

42. Phinney, R. E., The break-up of a turbulent liquid jet in a gaseous atmosphere, *Journal of Fluid Mech.*, Vol. 60, 1973, pp. 689-701.

43. Hoyt, J. W., Taylor, J. J., Waves on water jets, *Journal of Fluid Mech.*, Vol. 83, 1977, pp. 119-127

44. Lefebvre, A. H., *Atomization and Spray*

45. Di Wu, Delphine Guillemin, Andre W. Marshall, A modeling basis for predicting the initial sprinkler spray, *Fire Safety Journal*, Vol. 42, 2007, pp. 283-294.

46. FLUENT6.2 Userguide

47. Malvern EPCS Software Manual

48. FDS4 Userguide